

# Measurement of the electron charge asymmetry in $p\bar{p} \rightarrow W + X \rightarrow e\nu + X$ decays in $p\bar{p}$ collisions at $\sqrt{s} = 1.96$ TeV

V.M. Abazov,<sup>31</sup> B. Abbott,<sup>67</sup> B.S. Acharya,<sup>25</sup> M. Adams,<sup>46</sup> T. Adams,<sup>44</sup> J.P. Agnew,<sup>41</sup> G.D. Alexeev,<sup>31</sup> G. Alkhazov,<sup>35</sup> A. Alton<sup>a, 56</sup> A. Askew,<sup>44</sup> S. Atkins,<sup>54</sup> K. Augsten,<sup>7</sup> C. Avila,<sup>5</sup> F. Badaud,<sup>10</sup> L. Bagby,<sup>45</sup> B. Baldin,<sup>45</sup> D.V. Bandurin,<sup>73</sup> S. Banerjee,<sup>25</sup> E. Barberis,<sup>55</sup> P. Baringer,<sup>53</sup> J.F. Bartlett,<sup>45</sup> U. Bassler,<sup>15</sup> V. Bazterra,<sup>46</sup> A. Bean,<sup>53</sup> M. Begalli,<sup>2</sup> L. Bellantoni,<sup>45</sup> S.B. Beri,<sup>23</sup> G. Bernardi,<sup>14</sup> R. Bernhard,<sup>19</sup> I. Bertram,<sup>39</sup> M. Besançon,<sup>15</sup> R. Beuselinck,<sup>40</sup> P.C. Bhat,<sup>45</sup> S. Bhatia,<sup>58</sup> V. Bhatnagar,<sup>23</sup> G. Blazey,<sup>47</sup> S. Blessing,<sup>44</sup> K. Bloom,<sup>59</sup> A. Boehnlein,<sup>45</sup> D. Boline,<sup>64</sup> E.E. Boos,<sup>33</sup> G. Borissov,<sup>39</sup> M. Borysova<sup>l, 38</sup> A. Brandt,<sup>70</sup> O. Brandt,<sup>20</sup> R. Brock,<sup>57</sup> A. Bross,<sup>45</sup> D. Brown,<sup>14</sup> X.B. Bu,<sup>45</sup> M. Buehler,<sup>45</sup> V. Buescher,<sup>21</sup> V. Bunichev,<sup>33</sup> S. Burdin<sup>b, 39</sup> C.P. Buszello,<sup>37</sup> E. Camacho-Pérez,<sup>28</sup> B.C.K. Casey,<sup>45</sup> H. Castilla-Valdez,<sup>28</sup> S. Caughron,<sup>57</sup> S. Chakrabarti,<sup>64</sup> K.M. Chan,<sup>51</sup> A. Chandra,<sup>72</sup> E. Chapon,<sup>15</sup> G. Chen,<sup>53</sup> S.W. Cho,<sup>27</sup> S. Choi,<sup>27</sup> B. Choudhary,<sup>24</sup> S. Cihangir,<sup>45</sup> D. Claes,<sup>59</sup> J. Clutter,<sup>53</sup> M. Cooke<sup>k, 45</sup> W.E. Cooper,<sup>45</sup> M. Corcoran,<sup>72</sup> F. Couderc,<sup>15</sup> M.-C. Cousinou,<sup>12</sup> D. Cutts,<sup>69</sup> A. Das,<sup>42</sup> G. Davies,<sup>40</sup> S.J. de Jong,<sup>29, 30</sup> E. De La Cruz-Burelo,<sup>28</sup> F. Déliot,<sup>15</sup> R. Demina,<sup>63</sup> D. Denisov,<sup>45</sup> S.P. Denisov,<sup>34</sup> S. Desai,<sup>45</sup> C. Deterre<sup>c, 41</sup> K. DeVaughan,<sup>59</sup> H.T. Diehl,<sup>45</sup> M. Diesburg,<sup>45</sup> P.F. Ding,<sup>41</sup> A. Dominguez,<sup>59</sup> A. Dubey,<sup>24</sup> L.V. Dudko,<sup>33</sup> A. Duperrin,<sup>12</sup> S. Dutt,<sup>23</sup> M. Eads,<sup>47</sup> D. Edmunds,<sup>57</sup> J. Ellison,<sup>43</sup> V.D. Elvira,<sup>45</sup> Y. Enari,<sup>14</sup> H. Evans,<sup>49</sup> V.N. Evdokimov,<sup>34</sup> A. Fauré,<sup>15</sup> L. Feng,<sup>47</sup> T. Ferbel,<sup>63</sup> F. Fiedler,<sup>21</sup> F. Filthaut,<sup>29, 30</sup> W. Fisher,<sup>57</sup> H.E. Fisk,<sup>45</sup> M. Fortner,<sup>47</sup> H. Fox,<sup>39</sup> S. Fuess,<sup>45</sup> P.H. Garbincius,<sup>45</sup> A. Garcia-Bellido,<sup>63</sup> J.A. García-González,<sup>28</sup> V. Gavrilov,<sup>32</sup> W. Geng,<sup>12, 57</sup> C.E. Gerber,<sup>46</sup> Y. Gershtein,<sup>60</sup> G. Ginther,<sup>45, 63</sup> O. Gogota,<sup>38</sup> G. Golovanov,<sup>31</sup> P.D. Grannis,<sup>64</sup> S. Greder,<sup>16</sup> H. Greenlee,<sup>45</sup> G. Grenier,<sup>17</sup> Ph. Gris,<sup>10</sup> J.-F. Grivaz,<sup>13</sup> A. Grohsjean<sup>c, 15</sup> S. Grünendahl,<sup>45</sup> M.W. Grünewald,<sup>26</sup> T. Guillemín,<sup>13</sup> G. Gutierrez,<sup>45</sup> P. Gutierrez,<sup>67</sup> J. Haley,<sup>68</sup> L. Han,<sup>4</sup> K. Harder,<sup>41</sup> A. Harel,<sup>63</sup> J.M. Hauptman,<sup>52</sup> J. Hays,<sup>40</sup> T. Head,<sup>41</sup> T. Hebbeker,<sup>18</sup> D. Hedin,<sup>47</sup> H. Hegab,<sup>68</sup> A.P. Heinson,<sup>43</sup> U. Heintz,<sup>69</sup> C. Hensel,<sup>1</sup> I. Heredia-De La Cruz<sup>d, 28</sup> K. Herner,<sup>45</sup> G. Hesketh<sup>f, 41</sup> M.D. Hildreth,<sup>51</sup> R. Hirosky,<sup>73</sup> T. Hoang,<sup>44</sup> J.D. Hobbs,<sup>64</sup> B. Hoeneisen,<sup>9</sup> J. Hogan,<sup>72</sup> M. Hohlfield,<sup>21</sup> J.L. Holzbauer,<sup>58</sup> I. Howley,<sup>70</sup> Z. Hubacek,<sup>7, 15</sup> V. Hynek,<sup>7</sup> I. Iashvili,<sup>62</sup> Y. Ilchenko,<sup>71</sup> R. Illingworth,<sup>45</sup> A.S. Ito,<sup>45</sup> S. Jabeen<sup>m, 45</sup> M. Jaffré,<sup>13</sup> A. Jayasinghe,<sup>67</sup> M.S. Jeong,<sup>27</sup> R. Jesik,<sup>40</sup> P. Jiang,<sup>4</sup> K. Johns,<sup>42</sup> E. Johnson,<sup>57</sup> M. Johnson,<sup>45</sup> A. Jonckheere,<sup>45</sup> P. Jonsson,<sup>40</sup> J. Joshi,<sup>43</sup> A.W. Jung,<sup>45</sup> A. Juste,<sup>36</sup> E. Kajfasz,<sup>12</sup> D. Karmanov,<sup>33</sup> I. Katsanos,<sup>59</sup> M. Kaur,<sup>23</sup> R. Kehoe,<sup>71</sup> S. Kermiche,<sup>12</sup> N. Khalatyan,<sup>45</sup> A. Khanov,<sup>68</sup> A. Kharchilava,<sup>62</sup> Y.N. Kharzheev,<sup>31</sup> I. Kiselevich,<sup>32</sup> J.M. Kohli,<sup>23</sup> A.V. Kozelov,<sup>34</sup> J. Kraus,<sup>58</sup> A. Kumar,<sup>62</sup> A. Kupco,<sup>8</sup> T. Kurča,<sup>17</sup> V.A. Kuzmin,<sup>33</sup> S. Lammers,<sup>49</sup> P. Lebrun,<sup>17</sup> H.S. Lee,<sup>27</sup> S.W. Lee,<sup>52</sup> W.M. Lee,<sup>45</sup> X. Lei,<sup>42</sup> J. Lellouch,<sup>14</sup> D. Li,<sup>14</sup> H. Li,<sup>73</sup> L. Li,<sup>43</sup> Q.Z. Li,<sup>45</sup> J.K. Lim,<sup>27</sup> D. Lincoln,<sup>45</sup> J. Linnemann,<sup>57</sup> V.V. Lipaev,<sup>34</sup> R. Lipton,<sup>45</sup> H. Liu,<sup>71</sup> Y. Liu,<sup>4</sup> A. Lobodenko,<sup>35</sup> M. Lokajicek,<sup>8</sup> R. Lopes de Sa,<sup>45</sup> R. Luna-Garcia<sup>g, 28</sup> A.L. Lyon,<sup>45</sup> A.K.A. Maciel,<sup>1</sup> R. Madar,<sup>19</sup> R. Magaña-Villalba,<sup>28</sup> S. Malik,<sup>59</sup> V.L. Malyshev,<sup>31</sup> J. Mansour,<sup>20</sup> J. Martínez-Ortega,<sup>28</sup> R. McCarthy,<sup>64</sup> C.L. McGivern,<sup>41</sup> M.M. Meijer,<sup>29, 30</sup> A. Melnitchouk,<sup>45</sup> D. Menezes,<sup>47</sup> P.G. Mercadante,<sup>3</sup> M. Merkin,<sup>33</sup> A. Meyer,<sup>18</sup> J. Meyer<sup>i, 20</sup> F. Miconi,<sup>16</sup> N.K. Mondal,<sup>25</sup> M. Mulhearn,<sup>73</sup> E. Nagy,<sup>12</sup> M. Narain,<sup>69</sup> R. Nayyar,<sup>42</sup> H.A. Neal,<sup>56</sup> J.P. Negret,<sup>5</sup> P. Neustroev,<sup>35</sup> H.T. Nguyen,<sup>73</sup> T. Nunnemann,<sup>22</sup> J. Orduna,<sup>72</sup> N. Osman,<sup>12</sup> J. Osta,<sup>51</sup> A. Pal,<sup>70</sup> N. Parashar,<sup>50</sup> V. Parihar,<sup>69</sup> S.K. Park,<sup>27</sup> R. Partridge<sup>e, 69</sup> N. Parua,<sup>49</sup> A. Patwa<sup>j, 65</sup> B. Penning,<sup>45</sup> M. Perfilov,<sup>33</sup> Y. Peters,<sup>41</sup> K. Petridis,<sup>41</sup> G. Petrillo,<sup>63</sup> P. Pétróff,<sup>13</sup> M.-A. Pleier,<sup>65</sup> V.M. Podstavkov,<sup>45</sup> A.V. Popov,<sup>34</sup> M. Prewitt,<sup>72</sup> D. Price,<sup>41</sup> N. Prokopenko,<sup>34</sup> J. Qian,<sup>56</sup> A. Quadt,<sup>20</sup> B. Quinn,<sup>58</sup> P.N. Ratoff,<sup>39</sup> I. Razumov,<sup>34</sup> I. Ripp-Baudot,<sup>16</sup> F. Rizatdinova,<sup>68</sup> M. Rominsky,<sup>45</sup> A. Ross,<sup>39</sup> C. Royon,<sup>15</sup> P. Rubinov,<sup>45</sup> R. Ruchti,<sup>51</sup> G. Sajot,<sup>11</sup> A. Sánchez-Hernández,<sup>28</sup> M.P. Sanders,<sup>22</sup> A.S. Santos<sup>h, 1</sup> G. Savage,<sup>45</sup> M. Savitskyi,<sup>38</sup> L. Sawyer,<sup>54</sup> T. Scanlon,<sup>40</sup> R.D. Schamberger,<sup>64</sup> Y. Scheglov,<sup>35</sup> H. Schellman,<sup>48</sup> C. Schwanenberger,<sup>41</sup> R. Schwienhorst,<sup>57</sup> J. Sekaric,<sup>53</sup> H. Severini,<sup>67</sup> E. Shabalina,<sup>20</sup> V. Shary,<sup>15</sup> S. Shaw,<sup>41</sup> A.A. Shchukin,<sup>34</sup> V. Simak,<sup>7</sup> P. Skubic,<sup>67</sup> P. Slatery,<sup>63</sup> D. Smirnov,<sup>51</sup> G.R. Snow,<sup>59</sup> J. Snow,<sup>66</sup> S. Snyder,<sup>65</sup> S. Söldner-Rembold,<sup>41</sup> L. Sonnenschein,<sup>18</sup> K. Soustruznik,<sup>6</sup> J. Stark,<sup>11</sup> D.A. Stoyanova,<sup>34</sup> M. Strauss,<sup>67</sup> L. Suter,<sup>41</sup> P. Svoisky,<sup>67</sup> M. Titov,<sup>15</sup> V.V. Tokmenin,<sup>31</sup> Y.-T. Tsai,<sup>63</sup> D. Tsybychev,<sup>64</sup> B. Tuchming,<sup>15</sup> C. Tully,<sup>61</sup> L. Uvarov,<sup>35</sup> S. Uvarov,<sup>35</sup> S. Uzunyan,<sup>47</sup> R. Van Kooten,<sup>49</sup> W.M. van Leeuwen,<sup>29</sup> N. Varelas,<sup>46</sup> E.W. Varnes,<sup>42</sup> I.A. Vasilyev,<sup>34</sup> A.Y. Verkheev,<sup>31</sup> L.S. Vertogradov,<sup>31</sup> M. Verzocchi,<sup>45</sup> M. Vesterinen,<sup>41</sup> D. Vilanova,<sup>15</sup> P. Vokac,<sup>7</sup> H.D. Wahl,<sup>44</sup> M.H.L.S. Wang,<sup>45</sup> J. Warchol,<sup>51</sup> G. Watts,<sup>74</sup> M. Wayne,<sup>51</sup> J. Weichert,<sup>21</sup> L. Welty-Rieger,<sup>48</sup> M.R.J. Williams<sup>n, 49</sup> G.W. Wilson,<sup>53</sup> M. Wobisch,<sup>54</sup> D.R. Wood,<sup>55</sup> T.R. Wyatt,<sup>41</sup> Y. Xie,<sup>45</sup> R. Yamada,<sup>45</sup> S. Yang,<sup>4</sup> T. Yasuda,<sup>45</sup> Y.A. Yatsunenko,<sup>31</sup> W. Ye,<sup>64</sup> Z. Ye,<sup>45</sup> H. Yin,<sup>45</sup> K. Yip,<sup>65</sup> S.W. Youn,<sup>45</sup> J.M. Yu,<sup>56</sup>

J. Zennaro,<sup>62</sup> T.G. Zhao,<sup>41</sup> B. Zhou,<sup>56</sup> J. Zhu,<sup>56</sup> M. Zielinski,<sup>63</sup> D. Zieminska,<sup>49</sup> and L. Zivkovic<sup>14</sup>

(The D0 Collaboration\*)

<sup>1</sup>LAFEX, Centro Brasileiro de Pesquisas Físicas, Rio de Janeiro, Brazil

<sup>2</sup>Universidade do Estado do Rio de Janeiro, Rio de Janeiro, Brazil

<sup>3</sup>Universidade Federal do ABC, Santo André, Brazil

<sup>4</sup>University of Science and Technology of China, Hefei, People's Republic of China

<sup>5</sup>Universidad de los Andes, Bogotá, Colombia

<sup>6</sup>Charles University, Faculty of Mathematics and Physics,

Center for Particle Physics, Prague, Czech Republic

<sup>7</sup>Czech Technical University in Prague, Prague, Czech Republic

<sup>8</sup>Institute of Physics, Academy of Sciences of the Czech Republic, Prague, Czech Republic

<sup>9</sup>Universidad San Francisco de Quito, Quito, Ecuador

<sup>10</sup>LPC, Université Blaise Pascal, CNRS/IN2P3, Clermont, France

<sup>11</sup>LPSC, Université Joseph Fourier Grenoble 1, CNRS/IN2P3,

Institut National Polytechnique de Grenoble, Grenoble, France

<sup>12</sup>CPPM, Aix-Marseille Université, CNRS/IN2P3, Marseille, France

<sup>13</sup>LAL, Université Paris-Sud, CNRS/IN2P3, Orsay, France

<sup>14</sup>LPNHE, Universités Paris VI and VII, CNRS/IN2P3, Paris, France

<sup>15</sup>CEA, Irfu, SPP, Saclay, France

<sup>16</sup>IPHC, Université de Strasbourg, CNRS/IN2P3, Strasbourg, France

<sup>17</sup>IPNL, Université Lyon 1, CNRS/IN2P3, Villeurbanne, France and Université de Lyon, Lyon, France

<sup>18</sup>III. Physikalisches Institut A, RWTH Aachen University, Aachen, Germany

<sup>19</sup>Physikalisches Institut, Universität Freiburg, Freiburg, Germany

<sup>20</sup>II. Physikalisches Institut, Georg-August-Universität Göttingen, Göttingen, Germany

<sup>21</sup>Institut für Physik, Universität Mainz, Mainz, Germany

<sup>22</sup>Ludwig-Maximilians-Universität München, München, Germany

<sup>23</sup>Panjab University, Chandigarh, India

<sup>24</sup>Delhi University, Delhi, India

<sup>25</sup>Tata Institute of Fundamental Research, Mumbai, India

<sup>26</sup>University College Dublin, Dublin, Ireland

<sup>27</sup>Korea Detector Laboratory, Korea University, Seoul, Korea

<sup>28</sup>CINVESTAV, Mexico City, Mexico

<sup>29</sup>Nikhef, Science Park, Amsterdam, the Netherlands

<sup>30</sup>Radboud University Nijmegen, Nijmegen, the Netherlands

<sup>31</sup>Joint Institute for Nuclear Research, Dubna, Russia

<sup>32</sup>Institute for Theoretical and Experimental Physics, Moscow, Russia

<sup>33</sup>Moscow State University, Moscow, Russia

<sup>34</sup>Institute for High Energy Physics, Protvino, Russia

<sup>35</sup>Petersburg Nuclear Physics Institute, St. Petersburg, Russia

<sup>36</sup>Institució Catalana de Recerca i Estudis Avançats (ICREA) and Institut de Física d'Altes Energies (IFAE), Barcelona, Spain

<sup>37</sup>Uppsala University, Uppsala, Sweden

<sup>38</sup>Taras Shevchenko National University of Kyiv, Kiev, Ukraine

<sup>39</sup>Lancaster University, Lancaster LA1 4YB, United Kingdom

<sup>40</sup>Imperial College London, London SW7 2AZ, United Kingdom

<sup>41</sup>The University of Manchester, Manchester M13 9PL, United Kingdom

<sup>42</sup>University of Arizona, Tucson, Arizona 85721, USA

<sup>43</sup>University of California Riverside, Riverside, California 92521, USA

<sup>44</sup>Florida State University, Tallahassee, Florida 32306, USA

<sup>45</sup>Fermi National Accelerator Laboratory, Batavia, Illinois 60510, USA

<sup>46</sup>University of Illinois at Chicago, Chicago, Illinois 60607, USA

<sup>47</sup>Northern Illinois University, DeKalb, Illinois 60115, USA

<sup>48</sup>Northwestern University, Evanston, Illinois 60208, USA

<sup>49</sup>Indiana University, Bloomington, Indiana 47405, USA

<sup>50</sup>Purdue University Calumet, Hammond, Indiana 46323, USA

<sup>51</sup>University of Notre Dame, Notre Dame, Indiana 46556, USA

<sup>52</sup>Iowa State University, Ames, Iowa 50011, USA

<sup>53</sup>University of Kansas, Lawrence, Kansas 66045, USA

<sup>54</sup>Louisiana Tech University, Ruston, Louisiana 71272, USA

<sup>55</sup>Northeastern University, Boston, Massachusetts 02115, USA

<sup>56</sup>University of Michigan, Ann Arbor, Michigan 48109, USA

<sup>57</sup>Michigan State University, East Lansing, Michigan 48824, USA

<sup>58</sup>University of Mississippi, University, Mississippi 38677, USA

<sup>59</sup>University of Nebraska, Lincoln, Nebraska 68588, USA

- <sup>60</sup>Rutgers University, Piscataway, New Jersey 08855, USA  
<sup>61</sup>Princeton University, Princeton, New Jersey 08544, USA  
<sup>62</sup>State University of New York, Buffalo, New York 14260, USA  
<sup>63</sup>University of Rochester, Rochester, New York 14627, USA  
<sup>64</sup>State University of New York, Stony Brook, New York 11794, USA  
<sup>65</sup>Brookhaven National Laboratory, Upton, New York 11973, USA  
<sup>66</sup>Langston University, Langston, Oklahoma 73050, USA  
<sup>67</sup>University of Oklahoma, Norman, Oklahoma 73019, USA  
<sup>68</sup>Oklahoma State University, Stillwater, Oklahoma 74078, USA  
<sup>69</sup>Brown University, Providence, Rhode Island 02912, USA  
<sup>70</sup>University of Texas, Arlington, Texas 76019, USA  
<sup>71</sup>Southern Methodist University, Dallas, Texas 75275, USA  
<sup>72</sup>Rice University, Houston, Texas 77005, USA  
<sup>73</sup>University of Virginia, Charlottesville, Virginia 22904, USA  
<sup>74</sup>University of Washington, Seattle, Washington 98195, USA

(Dated: December 09, 2014)

We present a measurement of the electron charge asymmetry in  $p\bar{p} \rightarrow W + X \rightarrow e\nu + X$  events at a center-of-mass energy of 1.96 TeV, using data corresponding to  $9.7 \text{ fb}^{-1}$  of integrated luminosity collected with the D0 detector at the Fermilab Tevatron Collider. The asymmetry is measured as a function of the electron pseudorapidity and is presented in five kinematic bins based on the electron transverse energy and the missing transverse energy in the event. The measured asymmetry is compared with next-to-leading-order predictions in perturbative quantum chromodynamics and provides accurate information for the determination of parton distribution functions of the proton. This is the most precise lepton charge asymmetry measurement to date.

PACS numbers: 12.15.Ji, 13.38.Be, 13.85.Qk, 14.60.Cd, 14.70.Fm

## I. INTRODUCTION

Parton distribution functions (PDFs) are essential elements for cross section calculations at a hadron collider, and many precision measurements are dominated by the systematic uncertainty from PDFs. However, PDFs are not directly calculable within the standard model (SM) and must be determined using experimental inputs, including a wide range of scattering processes. At the Fermilab Tevatron Collider, a proton-antiproton ( $p\bar{p}$ ) collider with a center-of-mass energy of 1.96 TeV, the measurement of the electron charge asymmetry in the  $p\bar{p} \rightarrow W + X$  process provides important information for the determination of PDFs, as it is sensitive to the valence  $u$  and  $d$  quark and corresponding antiquark PDF distributions. In  $p\bar{p}$  collisions,  $W^+$  ( $W^-$ ) bosons are produced primarily by the annihilation of valence quarks in

the proton and antiproton. Since  $u$  quarks on average carry more momentum than  $d$  quarks [1–3],  $W^+$  bosons tend to be boosted in the proton direction, while  $W^-$  bosons tend to be boosted in the antiproton direction. This results in a non-zero  $W$  boson production charge asymmetry, defined as

$$A(y_W) = \frac{\frac{d\sigma_{W^+}}{dy_W} - \frac{d\sigma_{W^-}}{dy_W}}{\frac{d\sigma_{W^+}}{dy_W} + \frac{d\sigma_{W^-}}{dy_W}}, \quad (1)$$

where  $d\sigma_{W^\pm}/dy_W$  is the differential cross section for  $W^\pm$  boson production, and  $y_W$  is the  $W$  boson rapidity [4].

The  $W$  boson can decay leptonically with a charged lepton and a neutrino in the final state. The neutrino's presence can be inferred from an imbalance of transverse energy in the calorimeter, referred to as missing transverse energy ( $\cancel{E}_T$ ). Reconstruction of the neutrino longitudinal momentum ( $p_z^\nu$ ) is not feasible due to the unknown longitudinal momentum of the initial state interacting partons. Without  $p_z^\nu$ , it is impossible to perform a direct measurement of the  $W$  boson charge asymmetry with traditional methods. Instead we use the lepton pseudorapidity ( $\eta$ ) [4] distribution which is a convolution of the  $W$  boson production charge asymmetry and the  $V - A$  structure of the  $W$  boson decay. With a good understanding of the  $V - A$  structure, the lepton charge asymmetry as a function of lepton pseudorapidity can be used to constrain PDFs. The comparison between the  $W$  boson charge asymmetry and the lepton charge asymmetry is shown in Fig. 1, using the Monte Carlo (MC) event generator RESBOS [5] with the CTEQ6.6 [6] central PDF set.

---

\*with visitors from <sup>a</sup>Augustana College, Sioux Falls, SD, USA, <sup>b</sup>The University of Liverpool, Liverpool, UK, <sup>c</sup>DESY, Hamburg, Germany, <sup>d</sup>Universidad Michoacana de San Nicolas de Hidalgo, Morelia, Mexico <sup>e</sup>SLAC, Menlo Park, CA, USA, <sup>f</sup>University College London, London, UK, <sup>g</sup>Centro de Investigacion en Computacion - IPN, Mexico City, Mexico, <sup>h</sup>Universidade Estadual Paulista, São Paulo, Brazil, <sup>i</sup>Karlsruher Institut für Technologie (KIT) - Steinbuch Centre for Computing (SCC), D-76128 Karlsruhe, Germany, <sup>j</sup>Office of Science, U.S. Department of Energy, Washington, D.C. 20585, USA, <sup>k</sup>American Association for the Advancement of Science, Washington, D.C. 20005, USA, <sup>l</sup>Kiev Institute for Nuclear Research, Kiev, Ukraine, <sup>m</sup>University of Maryland, College Park, Maryland 20742, USA and <sup>n</sup>European Organization for Nuclear Research (CERN), Geneva, Switzerland

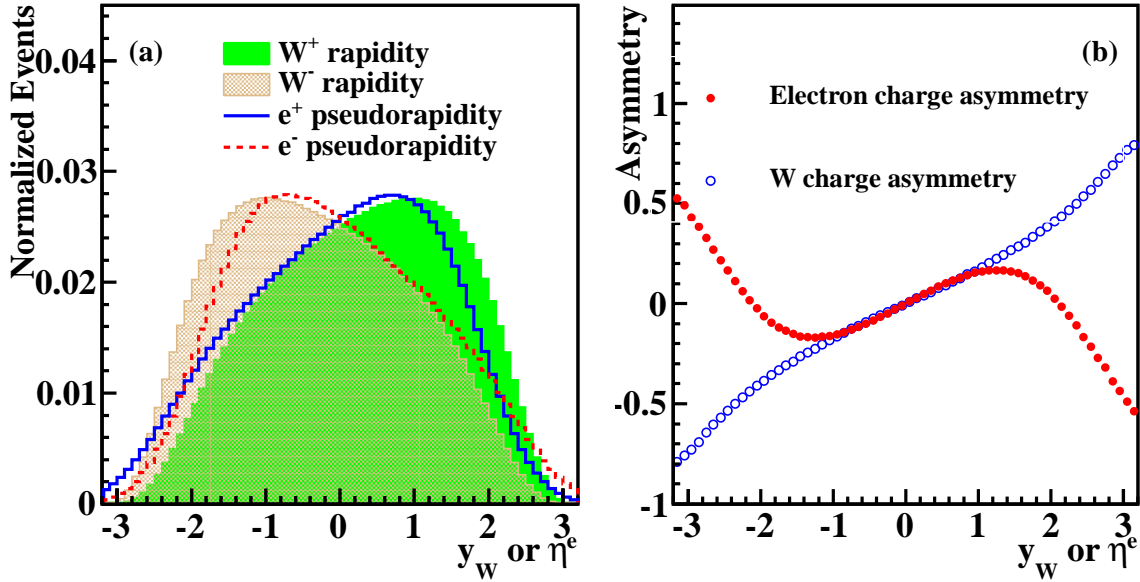


FIG. 1: (color online). (a) The  $W$  boson rapidity ( $y_W$ ) and electron pseudorapidity ( $\eta^e$ ) distributions in  $p\bar{p}$  collisions. (b) The charge asymmetry for the  $W$  boson and the decay electron. The electron asymmetry has a “turn-over” due to the convolution of the  $W$  boson asymmetry and the  $V - A$  structure of the  $W$  boson decay. These predictions were obtained using the MC event generator RESBOS [5] with the CTEQ6.6 [6] central PDF set, using the kinematic cuts  $p_T^e > 25$  GeV and  $p_T^W > 25$  GeV.

In the  $W \rightarrow e\nu$  decay mode used in this analysis, the experimentally measured  $W \rightarrow e\nu$  cross section times branching ratio as a function of electron pseudorapidity ( $\eta^e$ ) is

$$\sigma(\eta^e) \times Br(W \rightarrow e\nu) = \frac{N^e(\eta^e)}{\mathcal{L} \times \mathcal{A} \times \epsilon}, \quad (2)$$

where  $N^e(\eta^e)$  is the number of events with electron in the  $\eta^e$  bin,  $\mathcal{A}$  is the acceptance,  $\mathcal{L}$  is the integrated luminosity, and  $\epsilon$  is the selection efficiency. In the simplified case that the acceptances and efficiencies are the same for  $W^+$  and  $W^-$  bosons, the electron charge asymmetry,  $A$ , can be written using the numbers of electrons ( $N^{e^-}$ ) and positrons ( $N^{e^+}$ ) in each  $\eta^e$  bin as:

$$A(\eta^e) = \frac{N^{e^+}(\eta^e) - N^{e^-}(\eta^e)}{N^{e^+}(\eta^e) + N^{e^-}(\eta^e)}. \quad (3)$$

The lepton charge asymmetry in  $W$  boson decay has been measured by both the CDF [7–9] and D0 [10–12] Collaborations. The latest lepton charge asymmetry measurement from the D0 Collaboration was performed in the muon channel using  $7.3 \text{ fb}^{-1}$  of integrated luminosity [12]. The  $W$  boson asymmetry was extracted using missing transverse energy to estimate the neutrino direction, using  $1 \text{ fb}^{-1}$  of integrated luminosity by the CDF Collaboration [13] and  $10 \text{ fb}^{-1}$  by the D0 Collaboration [14]. The lepton asymmetry has also been measured at the Large Hadron Collider (LHC) in  $pp$  collisions

by the ATLAS [15] and CMS Collaborations [16] using integrated luminosities of  $35 \text{ pb}^{-1}$  and  $840 \text{ pb}^{-1}$ , respectively. At the LHC,  $W$  boson production is dominated by gluons and sea quarks, providing different information than the lepton asymmetry measured at the Tevatron.

In this analysis, we present a new measurement of the electron charge asymmetry based on data collected between April 2002 and September 2011 with the D0 detector at  $\sqrt{s} = 1.96 \text{ TeV}$ , corresponding to an integrated luminosity of  $9.7 \text{ fb}^{-1}$  [17]. We measure the electron charge asymmetry in five kinematic bins by selecting on the electron transverse energy ( $E_T^e$ ) and event  $\cancel{E}_T$ . Results from different kinematic bins probe different ranges of  $y_W$ , and thus different ranges of the fraction of proton momentum carried by the parton. There are three symmetric bins, ( $E_T^e > 25 \text{ GeV}$ ,  $\cancel{E}_T > 25 \text{ GeV}$ ), ( $25 < E_T^e < 35 \text{ GeV}$ ,  $25 < \cancel{E}_T < 35 \text{ GeV}$ ), ( $E_T^e > 35 \text{ GeV}$ ,  $\cancel{E}_T > 35 \text{ GeV}$ ) and two asymmetric bins, ( $25 < E_T^e < 35 \text{ GeV}$ ,  $\cancel{E}_T > 25 \text{ GeV}$ ), ( $E_T^e > 35 \text{ GeV}$ ,  $\cancel{E}_T > 25 \text{ GeV}$ ). With more data than in previous measurements and more data in the high pseudorapidity region, we provide information about the PDFs for a broader  $x$  range ( $0.002 < x < 0.99$  for  $|\eta^e| < 3.2$ ) at high  $Q^2 \approx M_W^2$ , where  $x$  is the fraction of the proton momentum carried by the colliding parton,  $Q^2$  is the momentum scale squared, and  $M_W$  is the  $W$  boson mass. This analysis improves upon and supersedes the previous D0 electron charge asymmetry result [11]. That result did not include the improved detector level calibrations discussed in Sec. IV E and Sec. IV F. In addition, it did not include MC modeling of the difference in

efficiency for electrons and positrons for different polarities of the solenoidal magnet surrounding the tracking region. This article also provides details of the complementary analysis of Ref. [14] where the  $W$  boson charge asymmetry is measured using the same data set.

## II. APPARATUS

The D0 detector [18, 19] contains central tracking, calorimeter, and muon systems. The central tracking system includes a silicon microstrip tracker (SMT) and a central scintillating fiber tracker (CFT), both located within a 1.9 T superconducting solenoidal magnet, with designs optimized for tracking and vertexing at pseudorapidity  $|\eta_{\text{det}}| < 3$  and  $|\eta_{\text{det}}| < 2.5$  [4], respectively, as shown in Fig. 2. Three liquid-argon and uranium calorimeters provide coverage of  $|\eta_{\text{det}}| < 3.5$  for electrons. The central calorimeter (CC) contains the region  $|\eta_{\text{det}}| < 1.1$ , and two end calorimeters (EC) extend coverage to  $1.5 < |\eta_{\text{det}}| < 3.5$ , as shown in Fig. 3. In the region  $1.0 < |\eta_{\text{det}}| < 1.5$ , particles cross multiple cryostat walls resulting in deterioration of the electron response. Each calorimeter consists of an inner electromagnetic section (EM) followed by a hadronic section. The EM calorimeter has four longitudinal layers with transverse segmentation of  $\Delta\eta \times \Delta\phi = 0.1 \times 0.1$ , except for the third layer, where it is  $0.05 \times 0.05$ . The outer muon system consists of a layer of tracking detectors and scintillation trigger counters in front of 1.9 T iron toroids, followed by two similar layers after the toroids, with a coverage of  $|\eta_{\text{det}}| < 2$ . The direction of the D0 solenoid and toroid magnetic fields were reversed periodically during data taking.

The D0 trigger is based on a three-level system. The first level consists of hardware and firmware components, and the second level combines information from specific subdetectors to construct a trigger decision based on physics quantities. The software-based third level processes the full event information using simplified versions of the offline reconstruction algorithms.

## III. EVENT SELECTION

The  $W \rightarrow e\nu$  events for this analysis are selected in several steps.

### A. Trigger selection

Candidate events must pass at least one of the calorimeter-based single EM triggers. The trigger towers in the calorimeter are  $0.2 \times 0.2$  in  $(\eta, \phi)$  space. At the third trigger level, the EM trigger objects must satisfy  $E_T^e(\text{trigger}) > 25$  GeV, or  $E_T^e(\text{trigger}) > 27$  GeV at higher instantaneous luminosity.

### B. Lepton transverse energy selection

We require one EM shower with transverse energy  $E_T^e > 25$  GeV measured in the calorimeter, accompanied by  $\cancel{E}_T > 25$  GeV. In  $W$  boson events,  $\cancel{E}_T$  is calculated using the electron and the vector sum of the transverse components of the energy deposited in the calorimeter ( $u_T$ ) after subtracting the electron deposit, i.e.,  $\vec{\cancel{E}}_T = -(\vec{E}_T^e + \vec{u}_T)$ . We also require that the electron has  $E_T^e < 100$  GeV to ensure good charge identification using the momentum of the charged track, described below.

### C. Electron selection

The EM cluster must be in the CC with  $|\eta_{\text{det}}| < 1.1$  or in the EC range  $1.5 < |\eta_{\text{det}}| < 3.2$  to allow a precise measurement of its energy. Electron candidates must be located within the fiducial region of each of the 32 EM calorimeter modules, defined as  $0.1 < \phi_{\text{mod}} < 0.9$ , where  $\phi_{\text{mod}}$  is the fractional part of  $32 \cdot \phi_{\text{trk}}/2\pi$ . The electron energy must be isolated in the calorimeter with  $[E_{\text{tot}}(0.4) - E_{\text{EM}}(0.2)]/E_{\text{EM}}(0.2) < 0.15$  (0.10) for CC (EC) electrons, where  $E_{\text{tot}}(\mathcal{R})$  and  $E_{\text{EM}}(\mathcal{R})$  are the total energy and the energy deposited in the EM section, respectively, within a cone of radius  $\mathcal{R} = \sqrt{(\Delta\phi)^2 + (\Delta\eta)^2}$  around the electron direction. Electron candidates are further required to have at least 90% of their energy deposited in the EM section of the calorimeter and to have a shower shape (H-matrix) [20, 21] consistent with that expected for an electron.

Electron candidates are required to be spatially matched to a reconstructed track by requiring  $|\Delta\eta| < 0.05$  and  $|\Delta\phi| < 0.05$ , where  $|\Delta\eta|$  and  $|\Delta\phi|$  are the differences in  $\eta$  and  $\phi$  between the cluster centroid and the extrapolated track. To reduce the electron charge misidentification probability, the track is further required to be of good quality: the track transverse momentum ( $p_T^{\text{trk}}$ ) must be greater than 10 GeV, the track must pass the central track fitting quality requirement, and the distance of closest approach (dca) of the track to the beam spot in the plane transverse to the beam direction should be less than 0.02 cm. Because the CFT detector does not cover the entire  $\eta_{\text{det}}$  region used in the analysis, electrons are split into four categories: CC electrons with full CFT coverage, EC electrons with full CFT coverage, EC electrons with partial CFT coverage, and EC electrons without CFT coverage. Optimized track quality requirements are employed for the different track categories. For tracks with full CFT coverage, we require that the track must have at least two SMT hits and nine CFT hits. For tracks with partial CFT coverage, we require that the track must have at least two SMT hits and three CFT hits. Finally, for tracks without CFT coverage, we require that the track must have at least eight SMT hits and pass a track significance  $(\frac{1/p_T^{\text{trk}}}{\sigma(1/p_T^{\text{trk}})})$ .

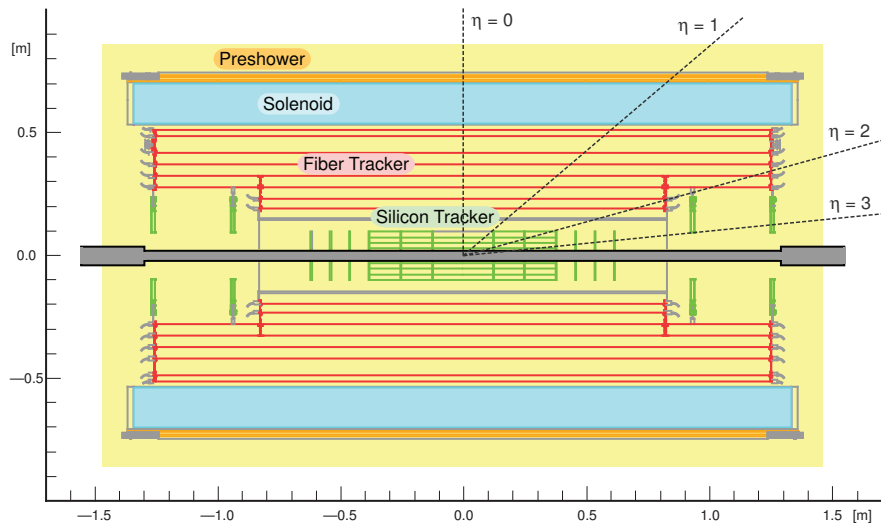


FIG. 2: (color online). Cross sectional view of the D0 central tracking detector in the  $x$ - $z$  plane.

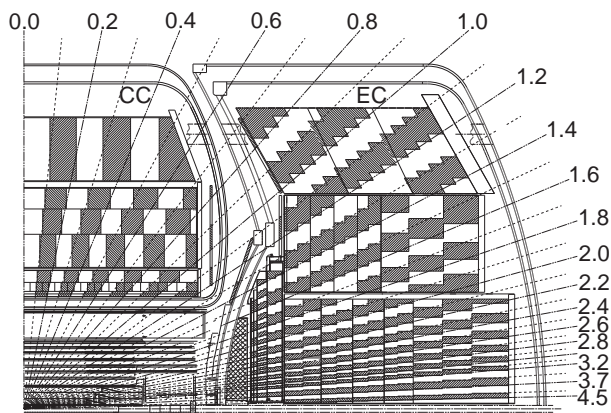


FIG. 3: Schematic view of a portion of the D0 calorimeters showing the transverse and longitudinal segmentation patterns. The rays indicate the pseudorapidity measured from the center of the detector ( $\eta_{\text{det}}$ ).

selection requirement, where  $\sigma(1/p_T^{\text{trk}})$  is the uncertainty on  $1/p_T^{\text{trk}}$  due to uncertainties on the tracking system hit positions.

#### D. $W$ boson event selection

Events are required to have a reconstructed  $p\bar{p}$  interaction vertex within 40 cm of the detector center along the  $z$  axis and a reconstructed  $W$  boson transverse mass of  $50 < M_T < 130$  GeV, where  $M_T = \sqrt{2E_T^e \cancel{E}_T(1 - \cos \Delta\phi)}$ , and  $\Delta\phi$  is the azimuthal angle between the electron and  $\vec{\cancel{E}}_T$ . We require  $u_T < 60$  GeV. The variable  $SET$  reflects the total activity in the calorimeter and is defined as the scalar sum of all of the transverse energy components measured by the calorimeter except those associated with electron.

Events are required to have either  $SET < 250$  GeV or  $SET < 500$  GeV, where the higher  $SET$  threshold is employed for the higher luminosity data-taking periods.

After applying the selection criteria described above, we retain 6,083,198  $W$  boson candidates. Of these, 4,466,735 are events with an electron in the CC region, and 1,616,463 have an electron in the EC region. The electron charge asymmetry is determined for each of the four electron categories based on CFT coverage and the results are then combined. Results from different data collection periods are found to be consistent with each other and are also combined. We assume charge parity (CP) invariance in the  $W$  boson production and decay, and thus report the folded asymmetry  $A(|\eta^e|) = \frac{1}{2} [A(\eta^e > 0) - A(\eta^e < 0)]$ . The electron charge asymmetries are measured in thirteen pseudorapidity bins in the range  $|\eta^e| < 3.2$ . The bin widths are chosen considering the statistics of the sample and the geometry of the detector. The selection criteria are identical to those employed in the  $W$  boson charge asymmetry paper, Ref. [14], which also used the entire Run II data set in the electron channel.

## IV. SIGNAL AND BACKGROUND SIMULATION

### A. Signal

MC simulations for the  $W \rightarrow e\nu$  process are generated using the PYTHIA [22] event generator with CTEQ6.1L PDFs [23], followed by a detailed GEANT-based simulation [24] of the D0 detector response and overlay of zero-bias events. Zero-bias events are selected from random beam crossings matching the instantaneous luminosity profile in the data. This simulation is then improved by correcting for known deficiencies in the detector model

and for higher-order effects not included in PYTHIA.

PYTHIA is a leading-order (LO) generator in which the modeling of the  $W$  boson  $p_T$  is not adequate for electroweak (EW) precision measurements. In order to improve the model of the  $W$  boson  $p_T$ , we derive a next-to-leading-order (NLO) correction from the ratio of RESBOS [5] with PHOTOS [25] (to simulate final state radiation, FSR) using the CTEQ6.6 central PDF set to PYTHIA with the CTEQ6.1L PDF set, as a function of the  $W$  boson  $p_T$  and rapidity.

## B. MC electron identification efficiency correction

The MC does not adequately describe the electron identification in the data, and the data and MC discrepancies as a function of  $\eta^e$  in the forward region are larger than they are in the central region.

$Z \rightarrow ee$  boson events from data and MC are used to calculate electron identification (EMID) corrections using a tag-and-probe method [21]. In this method, an electron candidate passing tight identification requirements is chosen as the tag electron, and then the probe electron is selected by requiring the invariant mass of the two electrons ( $M_{ee}$ ) to satisfy  $70 < M_{ee} < 110$  GeV. Probe electrons from this high purity, minimally biased electron sample are used to tune the MC selection efficiencies.

To remove the EMID differences between data and MC, we apply bin-by-bin efficiency corrections to the MC. There are multiple dependencies for the corrections, particularly for electrons in the forward region. In the procedure, the corrections are applied as functions of electron physical  $\eta^e$  (measured with the event vertex), electron detector  $\eta$  ( $\eta_{\text{det}}^e$ ), electron  $E_T^e$ , electron  $\phi$ , vertex position in the  $z$  direction ( $z_{\text{vtx}}$ ),  $SET$ , and instantaneous luminosity ( $L$ ) for three selections: the pre-selection (Pre-Selection, EM cluster isolation cut), calorimeter-based selection (Cal-ID), and track-based selection (Track-Match). As the number of selected  $Z \rightarrow ee$  events is limited, we perform a four-step iterative correction to reduce the selection differences between data and MC. As shown in Table I, we first derive a two-dimensional (2-D) correction to remove the two largest dependencies ( $\eta_{\text{det}}^e$  and  $E_T^e$ ). Then, using this 2-D correction, we examine the other parameters dependencies and develop a new 2-D correction to remove the largest two remaining dependencies. We iterate two more times until all EMID selection data-MC differences are greatly reduced. The electron  $\eta_{\text{det}}^e$  distributions of selected  $Z$  boson events before and after applying the EMID correction are shown in Fig. 4. Reasonable agreement is also observed for  $E_T^e$ ,  $\eta^e$ ,  $z_{\text{vtx}}$ ,  $\phi$ ,  $L$ ,  $SET$ , and  $M_{ee}$  distributions for selected  $Z$  boson events after applying EMID corrections.

TABLE I: Dependencies on the four steps used to determine EMID correction.

Step	Pre-Selection	Cal-ID/Track-Match
1	$\eta^e$	$\eta_{\text{det}}^e, E_T^e$
2		$\eta^e, z_{\text{vtx}}$
3		$\phi, L$
4		$SET, E_T^e$

## C. Electron trigger efficiency correction

We apply the trigger efficiency measured from data to the MC sample. To estimate the single EM trigger efficiency, we use  $Z \rightarrow ee$  data and apply the tag-and-probe method. The trigger efficiency correction is applied to MC events, as a function of  $E_T^e$  and  $\eta_{\text{det}}^e$ , separately for both CC and EC electrons.

## D. Positron/electron efficiency correction

The efficiencies for  $e^+$  and  $e^-$  identification in data and MC differ, with some difference for the two solenoid polarities also observed. The effect of different efficiencies for the two magnet polarities is ameliorated by the fact that the negative and positive solenoid polarity samples are nearly equal in size. For both data and MC, using a sample of  $Z \rightarrow e^+e^-$  events and a tag-and-probe method, we measure the identification efficiencies for all four combinations of particle charges ( $q$ ) and solenoid signs ( $p$ ), and calculate the data and MC efficiency ratio corrections ( $K_{\text{eff}}^{q,p}$ ) as a function of  $\eta^e$  and  $E_T$ . For each of these combinations, the MC events are reweighted to provide agreement with data. Figure 5 shows the comparison of MC and data after the correction for positrons with positive solenoid polarity.

## E. Electron energy tuning

The mismodeling of the passive material in front of the calorimeter results in energy mismeasurement for electrons. However, there are additional causes of electron energy mismeasurement. The interaction rate of proton and antiproton bunch crossings depends on instantaneous luminosity. Events with higher instantaneous luminosity may have more energy deposited in the calorimeter due to pile-up contributions. In addition, the  $SET$  will contribute to the electron energy measurement by adding from a few MeV to a few GeV to the electron energy. The electron energy reconstruction, especially in the forward region, has strong  $\eta_{\text{det}}^e$ , instantaneous luminosity, and  $SET$  dependences. The interplay of these three effects makes a precision measurement of the energy challenging. To derive a correction, we fit  $Z$  boson events



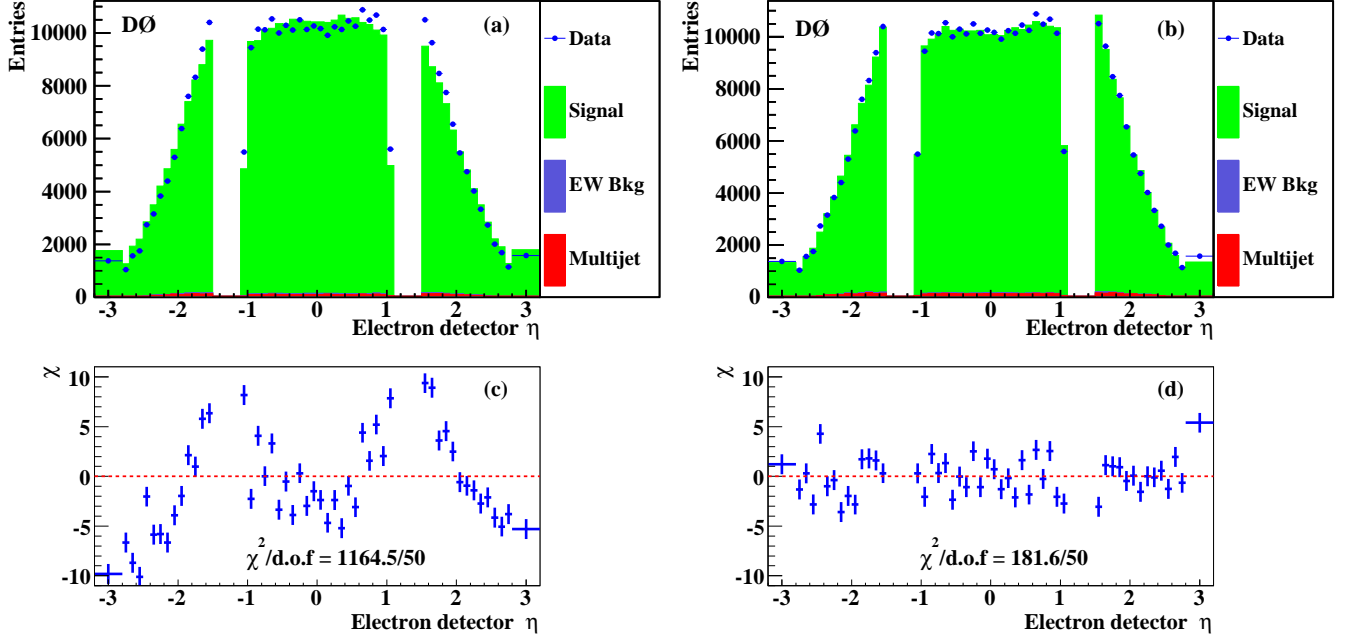


FIG. 4: (color online). Comparisons of the electron  $\eta_{\text{det}}^e$  distributions between data and the sum of signal and background predictions for selected Z boson events, (a) event distribution and (c) value of  $\chi_i$  for each bin between data and the MC predictions before applying the EMID correction, (b) event distribution and (d) value of  $\chi_i$  for each bin after applying the EMID correction.  $\chi_i = \Delta N_i / \sigma_{N_i}$ ,  $\Delta N_i$  is the difference between the number of data and that of the MC prediction, and  $\sigma_{N_i}$  is the statistical uncertainty in each  $\eta$  bin.

in different  $\eta_{\text{det}}^e$  bins using a VOIGT function [26] combined with an exponential background to obtain the Z boson mass peak position, and compare the mass peak position with the LEP value (91.1876 GeV) [27]. In the mass peak fitting, the multijet background and other SM backgrounds are subtracted. As shown in Fig. 6, there are deviations of more than 2 GeV in the value of the Z boson mass peak in the very forward bins before calibration.

An iterative method using MINUIT [28] fitting is employed to reduce the electron energy dependences on instantaneous luminosity, *SET* and  $\eta_{\text{det}}^e$ . The procedure includes:

- **Instantaneous luminosity tuning:** The dependence of the peak position of the Z boson mass on increasing luminosity includes several effects: (a) the addition of energy from pile-up and hadronic recoil energy in the electron reconstruction window, (b) the decrease of the energy response due to the high voltage drop on the resistive coating [18, 29] on the calorimeter electrodes due to the increased ionization at high luminosity, (c) and the decrease of the response due to the over-subtraction of the baseline of the signal shape in the calorimeter [29]. For MC, overlaid zero-bias events contribute to the energy of the electron, with high instantaneous luminosity causing a corresponding increase of the value of the Z boson peak position. Thus, differ-

ent correction factors in sixteen luminosity bins are applied to data and MC, according to the instantaneous luminosity of the event.

- **SET tuning:** The *SET* affects the electron energy by contributing additional energy to the electron shower. The correction factors in thirteen *SET* bins are developed and applied to data and MC, according to the *SET* of the event.
- **$\eta_{\text{det}}^e$  tuning:** For  $Z \rightarrow ee$  events, there are two electrons which will most likely be located at different  $\eta_{\text{det}}^e$  positions. When tuning the electron energy modeling for a specific  $\eta_{\text{det}}^e$  bin, the tuning is affected by electron energy modeling in other  $\eta_{\text{det}}^e$  bins, thus there are strong correlations between bins. The procedure employs 44 (CC) or 72 (EC) parameters (22  $\eta_{\text{det}}^e$  bins in the CC region, with scale ( $\alpha$ ) and offset ( $o$ ) parameters for each  $\eta_{\text{det}}^e$  bin, as  $E_{\text{cor}}^e = o + \alpha \times E^e$ , where  $E^e$  and  $E_{\text{cor}}^e$  are the electron energy before and after energy tuning. There are 24  $\eta_{\text{det}}^e$  bins in the EC region, with scale ( $\alpha$ ), offset ( $o$ ), and non-linearity ( $\gamma$ ) parameters for each  $\eta_{\text{det}}^e$  bin, as  $E_{\text{cor}}^e = o + \alpha \times E^e + \gamma \times (E^e)^2$ ). To take into account substantial differences in statistics between different  $\eta_{\text{det}}^e$  bins and to speed up the procedure, we employ iterative fitting instead of a global fit:

1. Fit the events in the  $\eta_{\text{det}}^e$  bin with the largest



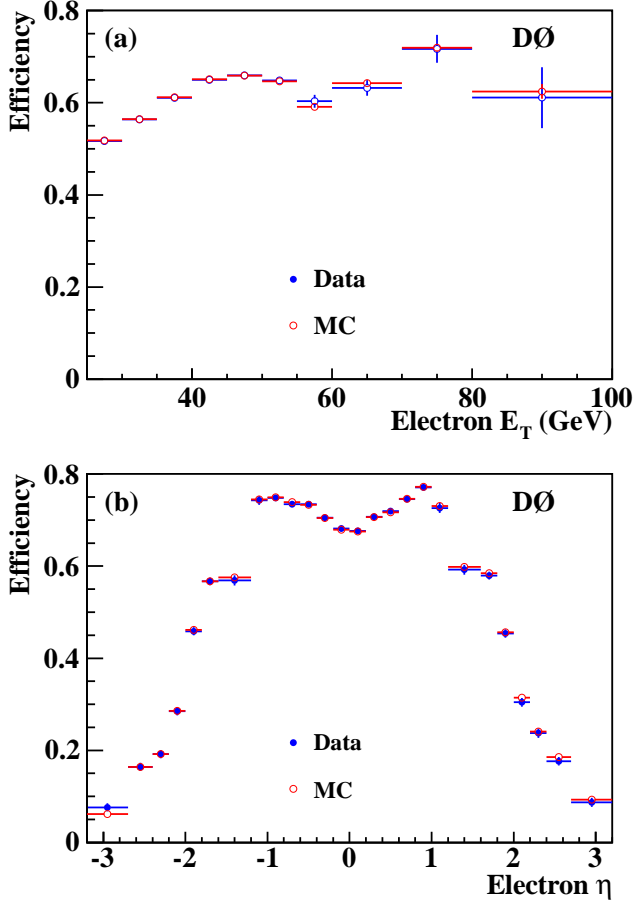


FIG. 5: (color online). Data and MC track matching efficiency comparison after  $K_{\text{eff}}^{q,p}$  correction, as a function of (a) electron  $E_T$  and (b) electron  $\eta$ , for  $e^+$  with positive solenoid polarity. There is an efficiency drop around 55 GeV, which comes from the tag-and-probe method, since in  $Z \rightarrow ee$  events, when the tagged electron has high  $E_T$ , the other electron in the event is soft, resulting in inefficiency in the EMID.

statistics (i.e.,  $0 < \eta_{\text{det}}^e < 0.1$  for CC electrons and  $1.5 < \eta_{\text{det}}^e < 1.6$  for EC electrons).

2. Fix the parameters for the  $\eta_{\text{det}}^e$  bin fit in the previous step, and then fit the events in the next  $\eta_{\text{det}}^e$  bin (i.e.,  $0.1 < \eta_{\text{det}}^e < 0.2$  for CC electrons and  $1.6 < \eta_{\text{det}}^e < 1.7$  for EC electrons).
3. Repeat Step 2 for each  $\eta_{\text{det}}^e$  bin.
4. Repeat Steps 1–3 until the fitting results become stable, with a minimum  $\chi^2$  value between the fitted  $Z$  boson mass peak values in each bin and that of the LEP value.

The position of the  $Z$  boson peak in bins of electron  $\eta_{\text{det}}^e$  before and after the electron energy tuning is shown in Fig. 6, demonstrating that good consistency is obtained between the LEP measured value [27] and the

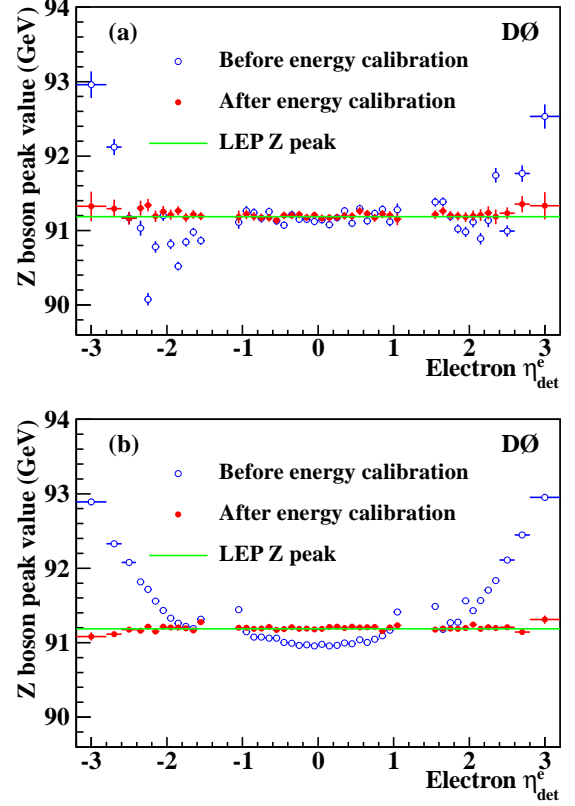


FIG. 6: (color online). The fitted mass value of CC-EC events (events with one electron in the CC and the other in the EC) in  $\eta_{\text{det}}^e$  bins for (a) data and (b) MC  $Z \rightarrow ee$  events. The open blue points are the  $Z$  boson mass peak values before applying the electron energy calibration, and the solid red points represent the peak values after applying the electron energy calibration.

fitted mass value of the  $Z$  boson mass peak after tuning.

After applying the electron energy scale correction, an additional energy smearing correction [21] is applied to the MC to achieve data-MC agreement for the energy resolution.

## F. Recoil system tuning

We also correct the energy response in MC for the hadrons recoiling against a  $W$  or  $Z$  boson. The recoil system model is needed to determine the  $\cancel{E}_T$  in  $W$  boson events and is a key component for the electron charge asymmetry measurement. The response of the calorimeter to the hadronic recoil differs from its response to objects which shower electromagnetically. This difference occurs because the hadronic calorimeter modules differ in construction from the electromagnetic modules and because the process by which hadrons interact in material is different from that of electrons and photons. In principle, if we knew the particle composition of the recoil, it

would be possible to simulate the overall recoil response. However, there is no reliable model to estimate from first principles the particle composition of the recoil system. Furthermore, many of the recoil particles have low momentum, and the energy scale corrections are difficult to calculate for low energy particles.

In this analysis, the hadronic response is directly determined from  $Z \rightarrow ee$  data by comparing the  $Z$  boson transverse momentum ( $p_T^Z$ ) measured from the electron pair ( $p_T^{ee}$ ) to that measured from the recoil system ( $u_T$ ). The particle composition in the  $W$  and  $Z$  boson recoil systems should be very similar, and by averaging over the  $Z$  boson sample, we expect to derive a hadronic response model that closely approximates that of the  $W$  boson sample.

To perform this comparison, a pair of coordinate axes in the transverse plane to the beam is used. As shown in Fig. 7, the  $\eta$  axis is defined as the inner bisector of the two electron transverse momentum directions, and the  $\xi$  axis is perpendicular to the  $\eta$  axis in the transverse plane. The  $\eta$  direction is defined using electron angle information only, therefore, the recoil projection in the  $\eta$  direction is minimally sensitive to the electron energy resolution. The projections onto the  $\eta$  and  $\xi$  axes are denoted  $p_{T\eta}^e$ ,  $p_{T\xi}^e$ ,  $u_{T\eta}$ , and  $u_{T\xi}$ . The projection of any transverse momentum  $\vec{p}_T$  onto these axes is

$$\vec{p}_T = p_{\eta}\hat{\eta} + p_{\xi}\hat{\xi}. \quad (4)$$

The  $\eta$  and  $\xi$  projections enable a good understanding of the hadronic response by comparing  $p_{T\eta}^{ee}$  with  $u_{T\eta}$ . The momentum vectors of the dielectron and hadron systems should be equal and opposite due to momentum conservation.

To improve the recoil modeling in the MC, we determine the hadronic scaling, smearing, and offset factors ( $\alpha$ ,  $\beta$ , and  $o$ ) to MC samples using MINUIT fitting, as

$$\begin{aligned} X_{\eta}^{\text{new}} &= \alpha \times [X_{\eta}^{\text{gen}} + (X_{\eta}^{\text{raw}} - X_{\eta}^{\text{gen}}) \times \beta] + o, \\ X_{\xi}^{\text{new}} &= \alpha \times [X_{\xi}^{\text{gen}} + (X_{\xi}^{\text{raw}} - X_{\xi}^{\text{gen}}) \times \beta] + o. \end{aligned} \quad (5)$$

In these equations,  $X$  represents the recoil momentum,  $X_{\eta}^{\text{new}}$  and  $X_{\xi}^{\text{new}}$  are the new recoil system projections in the  $\eta$  and  $\xi$  directions after recoil tuning,  $X_{\eta}^{\text{raw}}$  and  $X_{\xi}^{\text{raw}}$  are the recoil system projections in the  $\eta$  and  $\xi$  directions before recoil tuning, and  $X_{\eta}^{\text{gen}}$  and  $X_{\xi}^{\text{gen}}$  are the generator-level recoil system projections in the  $\eta$  and  $\xi$  directions. By varying  $\alpha$ ,  $\beta$ , and  $o$  in the MC, we achieve good agreement between the MC and data recoil system projections in both the  $\eta$  and  $\xi$  directions for each  $p_T^Z$  bin.

We also perform recoil tuning to eliminate  $SET$  dependencies. An iterative method is used to remove correlations between  $p_T^Z$  and  $SET$ , which is done by doing the recoil tuning in each  $SET$  bin, and then, based on the  $SET$  tuning, performing the tuning for each  $p_T^Z$  bin. We iterate these two steps until stable and consistent results are obtained.

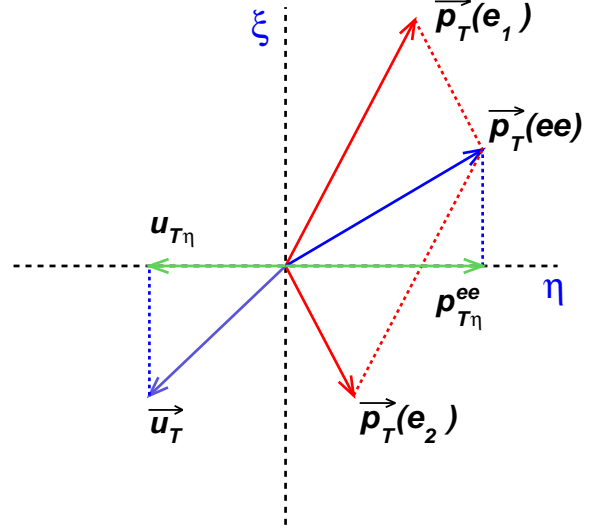


FIG. 7: (color online). Definitions of the  $\eta$  and  $\xi$  axes in  $Z \rightarrow ee$  events, and the dielectron and the hadronic recoil system projections in these axes. The  $\eta$ - $\xi$  plane is transverse to the beam.

Additionally, there is a top-bottom asymmetry in the D0 calorimeter coming from variations in the lengths of calorimeter signal cables. We use an additional correction based on the azimuthal angle of the recoil system to reproduce this asymmetry in the MC, and achieve agreement between data and MC.

### G. Charge misidentification

Misidentification of the charge sign of the electron would result in a dilution of the measured electron charge asymmetry. We measure the charge misidentification probability ( $Q_{\text{mis}}$ ) with  $Z \rightarrow ee$  events using the tag-and-probe method. The CC and EC electron charge misidentification probabilities are measured using CC-CC events (both electrons in the CC) and CC-EC events separately. In addition to the general electron selection criteria, we use a tighter track significance cut to choose tag electrons. This ensures that the track curvature is sufficiently well measured to enable a good measurement of the tag track charge. We determine the charge misidentification probabilities in the data and MC as functions of  $\eta^e$  and  $E_T^e$ . The charge misidentification probability in data averaged over  $E_T^e$  varies from 0.2% at  $|\eta^e| = 0$  to 8% at  $|\eta^e| = 3.0$ , as shown in Fig. 8.

The charge misidentification probability measured in data is roughly a factor of three larger than it is in MC, which is due to MC modeling of the tracking detector, including material modeling deficiencies, and tracking de-

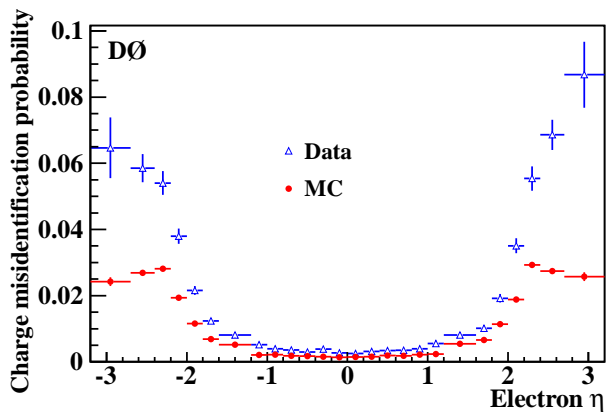


FIG. 8: (color online). Charge misidentification probability as a function of  $\eta^e$ . The blue triangles represent the measured data charge misidentification probability, and the red dots represent that of the MC.

tector alignment differences between MC and data. As a function of  $\eta^e$  and  $E_T^e$ , we flip the charge of electrons satisfying analysis criteria so that the charge misidentification probability of MC matches that of the data. This extra electron charge misidentification probability for each  $\eta^e$  and  $E_T^e$  bin is applied to the MC used in this analysis.

### H. Backgrounds

Background contributions, except multijet events, are estimated using the PYTHIA MC. This includes  $W \rightarrow \tau\nu$  events in which the  $\tau$  lepton decays to an electron and a neutrino,  $Z \rightarrow ee$  events in which one of the electrons is not identified, and  $Z \rightarrow \tau\tau$  events with one tau decaying to an electron and the other not identified. We normalize these background contributions according to their cross sections [30] and the integrated luminosity. In the  $W \rightarrow \tau\nu$  MC sample, the tau decay phase space and momentum is not modeled correctly in PYTHIA v6, and we use TAUOLA [31], which applies the correct branching fraction for each channel and correctly treats the tau polarization.

The largest background originates from multijet events in which one jet is misreconstructed as an electron and there is significant  $\cancel{E}_T$  in the event. Even though the probability for a jet to be misidentified as an electron is small due to the track requirements, multijet events are the dominant source of background in this analysis due to the large jet production cross section. The multijet background is estimated using collider data by fitting the  $W$  boson  $M_T$  distribution in the region 50 to 130 GeV (with other SM backgrounds subtracted) to the sum of the shape predicted by the  $W \rightarrow e\nu$  signal MC and the shape measured from a multijet-enriched sample. The multijet-enriched sample is selected by reversing the shower shape (H-matrix) requirement for the

electron candidates [32].

The background contributions are determined as a function of  $\eta^e$ , and the average contributions in the  $M_T$  range of 50 GeV to 130 GeV are 4.0% from multijet, 2.6% from  $Z \rightarrow ee$ , 2.2% from  $W \rightarrow \tau\nu$ , and 0.2% from  $Z \rightarrow \tau\tau$  events. The  $W \rightarrow \tau\nu$  boson background has the same production process as the signal, it contributes to the raw asymmetry measurement. For the  $Z$  boson background, the contribution is small. The charge of the fake electron in multijet events is random and thus there is no asymmetry in this background.

### I. Data and MC comparisons

Comparisons of the  $E_T^e$ ,  $\cancel{E}_T$ ,  $\eta_{\text{det}}^e$ , and  $W$  boson  $p_T$  of selected data events and the sum of the signal and background predictions are shown in Fig. 9. Reasonable agreement between data and prediction is observed for all distributions, but there are discrepancies between data and prediction, i.e., in the tail region of the  $\cancel{E}_T$  distribution, so we assign systematic uncertainties to account for those discrepancies.

## V. UNFOLDING

The electron and positron  $\eta^e$  distributions after event selection cannot be directly compared with generator-level predictions due to detector resolution and acceptance effects. To correct for the migration of events from one bin to another due to these effects, an unfolding procedure is performed before comparing the measured asymmetry with predictions.

### A. Migration unfolding

Bin purity is defined as the fraction of events in a bin  $i$  for any variable  $x$  that comes from events that were generated in that bin:

$$\pi(x, i) = \frac{N_{\text{Reco}}^{\text{Gen}}(x, i)}{N_{\text{Reco}}(x, i)}, \quad (6)$$

where  $N_{\text{Reco}}^{\text{Gen}}(x, i)$  is the number of events in bin  $i$  at both the generator and reconstruction-levels, and  $N_{\text{Reco}}(x, i)$  is the number of events in bin  $i$  at the reconstruction level. Our studies show that the migration between  $\eta^e$  bins is small, but that the migration between the five different kinematic bins in  $(E_T^e, \cancel{E}_T)$  is significant, with purities varying from 60% to 90%.

The event migration correction uses an unfolding procedure based on migration matrices determined using the  $W$  boson MC. The migration matrices are derived using an inclusive  $W \rightarrow e\nu$  sample generated using PYTHIA with the CTEQ6.1L PDF set. For each reconstruction-level kinematic bin, we construct relevant detector migration matrices for non-overlapping kinematic bins. These

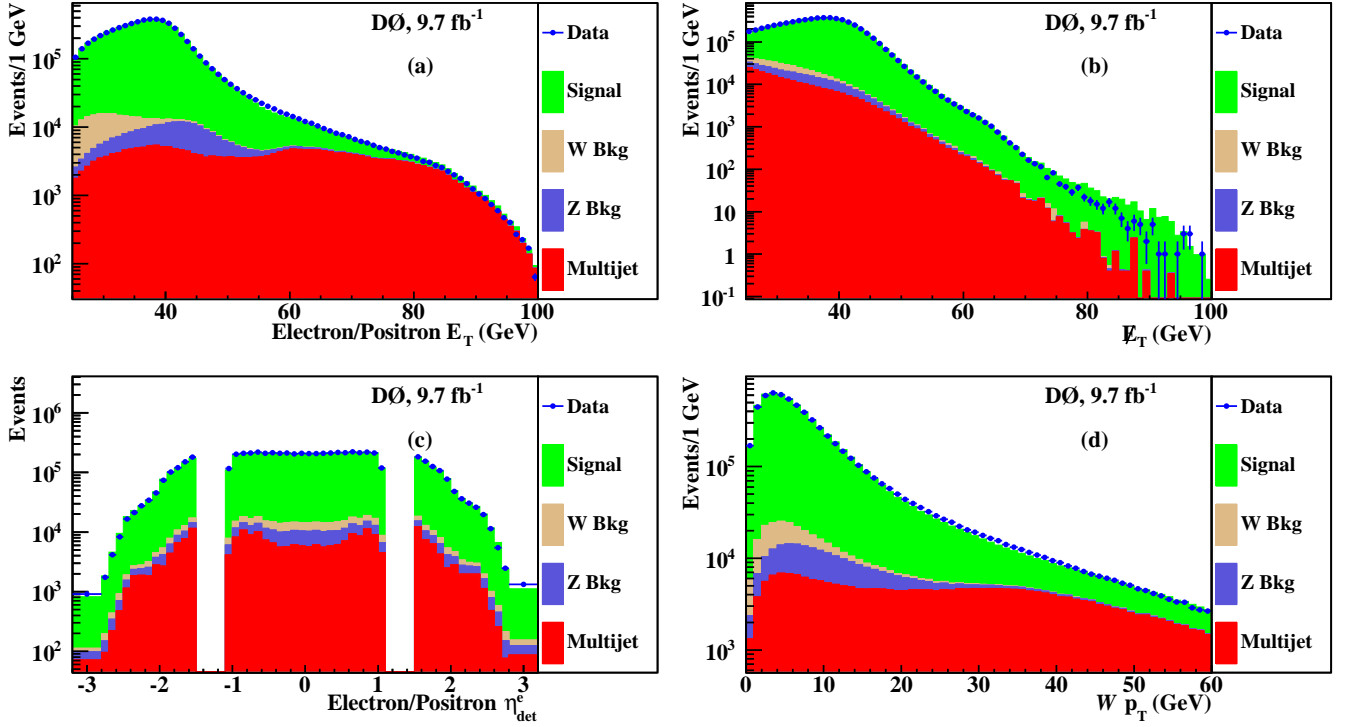


FIG. 9: (color online). Comparisons of electron (a)  $E_T^e$ , (b)  $E_T$ , (c)  $\eta_{\text{det}}^e$ , and (d)  $W$  boson  $p_T$  between data and the sum of signal and background predictions for selected  $W$  boson events. Systematic uncertainties are not shown.

matrices are used to describe events migrating from a given generator-level  $\eta^e$  and kinematic bin into a different reconstruction-level  $\eta^e$  and kinematic bin, as

$$M_{ij}^{AB} = \frac{N_{\text{Reco}, i, B}^{\text{Gen}, j, A}}{N_{\text{Reco}, i, B}} \quad (7)$$

which is the number of events in both the generator-level  $\eta^e$  bin  $j$  and kinematic bin  $A$  and in the reconstruction-level  $\eta^e$  bin  $i$  and kinematic bin  $B$  ( $N_{\text{Reco}, i, B}^{\text{Gen}, j, A}$ ), divided by the number of events in the reconstruction-level  $\eta^e$  bin  $i$  and kinematic bin  $B$  ( $N_{\text{Reco}, i, B}$ ).

Using the selected  $W$  boson MC events in each kinematic bin and the migration matrices, we build the connection between the events selected after reconstruction ( $N_{\text{Reco}}(\eta^e, i)$ ) and the generator-level events ( $N_{\text{Gen}(j)}^A$ ), and use the migration matrices to remove the detector resolution effects as

$$N_{\text{Gen}(j)}^A = \sum_B \sum_i N_{\text{Reco}}(\eta^e, i) \times M_{ij}^{AB}. \quad (8)$$

### B. Acceptance $\times$ efficiency correction

After correcting the MC for charge misidentification and migration, the electron-to-positron ratio at the reconstruction level is still different from that at the generator-level. The remaining differences come from ac-

ceptance times efficiency ( $\mathcal{A} \times \epsilon$ ) effects. An  $\mathcal{A} \times \epsilon$  correction is performed to account for acceptance and selection criteria effects. This correction is obtained for each  $\eta^e$  bin by accounting for the difference between the generator-level and unfolded reconstruction-level asymmetries (after charge misidentification and migration corrections).

## VI. CLOSURE TESTS

To verify the validity of the unfolding procedure, MC closure tests are performed with  $W \rightarrow e\nu$  events. At the generator level, the electron asymmetries for the five kinematic bins under consideration are obtained using simple kinematic cuts (i.e., electron transverse momentum  $p_T^e(\text{Gen}) > 25$  GeV and neutrino transverse momentum  $p_T^\nu(\text{Gen}) > 25$  GeV). At the reconstruction level with the detector simulation included, the electron asymmetries are extracted once again. Then, after applying the unfolding procedure to the reconstruction-level asymmetries, we expect that the unfolded asymmetries will match the generator-level asymmetries. We perform two closure tests to verify this is the case.

### A. Closure test I

In this closure test, half of the MC events are used to derive the migration matrices and  $\mathcal{A} \times \epsilon$  correction, and

the other half are used as pseudo data. This method avoids the bias of applying the corrections to the same sample used to develop the corrections. Good consistency between the unfolded asymmetry and the generator asymmetry is obtained for each kinematic bin. An example is shown in Fig. 10 which represents the test results for the  $E_T^e > 25$  GeV,  $\cancel{E}_T > 25$  GeV bin after CP folding.

### B. Closure test II

In this closure test, half of the MC events are used to study the migration matrices and  $\mathcal{A} \times \epsilon$  correction, and the other half are used as pseudo data, but with the asymmetry distribution modified at the generator level (enhanced or suppressed), as shown in Fig. 11. To modify the generator-level asymmetry, a reweighting factor based on  $\eta^e$  ( $f = 1 \pm 0.05 \times \eta^e$ ) is applied to the number of electrons only, while leaving the number of positrons unchanged.

Good agreement between the unfolded asymmetry and generator-modified asymmetry is obtained for each kinematic bin. The plots shown in Fig. 11 correspond to the test results for the  $E_T^e > 25$  GeV,  $\cancel{E}_T > 25$  GeV bin with CP-folding. This test confirms that the migration matrix and  $\mathcal{A} \times \epsilon$  corrections derived from the predicted asymmetry can be applied without bias for other asymmetries.

## VII. SYSTEMATIC UNCERTAINTIES

The systematic uncertainties of the electron charge asymmetry measurement in the five kinematic bins are summarized in Tables II–VI. Because this is an asymmetry measurement, some of the uncertainties cancel in the measured ratio, i.e., uncertainties from electron identification, energy calibration, recoil tuning, and background modeling are small compared with the uncertainties in the individual  $e^+$  and  $e^-$  distributions. The various sources of uncertainties that are considered are described below.

### A. Systematic uncertainty from the generator-level prediction

The modeling of the  $W$  boson  $p_T$  impacts the asymmetry measurements, and different generators give different predictions, even those at the same order (either LO and NLO). To estimate the uncertainty from the  $p_T^W$  modeling, we weight the  $p_T^W$  spectrum from the PYTHIA sample to match those distributions from the RESBOS [5] and POWHEG [33] generators, separately. Then we take the difference resulting from the two weightings as a systematic uncertainty.

At the generator level, any FSR electrons and photons within a cone of  $\Delta\mathcal{R} < 0.3$  around an electron are merged with the electron. To estimate the uncertainty from FSR, we weight the events with  $|M_{\text{Gen}} - M_{\text{Part}}| > 1$  GeV by  $\pm 10\%$ , where  $M_{\text{Gen}}$  and  $M_{\text{Part}}$  are the  $W$  boson mass at the generator and particle levels, respectively, and take the deviation of the asymmetry as the FSR uncertainty.

The  $p_T^W$  modeling and FSR uncertainties are combined in quadrature to form the overall generator uncertainty.

### B. Systematic uncertainty from EMID and trigger

To study the uncertainty from the EMID selection, we vary the efficiency correction factors by  $\pm 1$  standard deviation, extract the asymmetries with the varied EMID corrections, and take the larger variation in each bin as a symmetric systematic uncertainty in that bin. As expected, the largest contribution is from the track-match efficiency correction. Similarly, we obtain the systematic uncertainty from the single EM trigger efficiency modeling, and combine these two uncertainties in quadrature.

### C. Systematic uncertainty from $K_{\text{eff}}^{q,p}$

The uncertainty from  $K_{\text{eff}}^{q,p}$  correction is determined using the same procedure as for the determination of the uncertainty from EMID.

### D. Systematic uncertainty from electron energy tuning

To obtain agreement between the data and MC  $Z$  boson invariant mass distributions, we first perform the energy calibration for both data and MC, and then tune the MC with scale and smearing parameters. To study the uncertainty from these corrections, we vary each of the energy tuning parameters by  $\pm 1$  standard deviation, extract the asymmetries with the varied parameters, and take the larger variation in each bin as a symmetric systematic uncertainty in that bin. Finally, we combine the uncertainties of all contributing parameters in quadrature to arrive at one total electron energy tuning uncertainty. For this uncertainty study, we consider contributions from the energy scale, smearing, offset, and non-linearity terms.

### E. Systematic uncertainty from recoil modeling

The uncertainty due to the recoil modeling is determined using the same procedure as the determination of the uncertainty from the electron energy tuning. We consider contributions from scale, smearing, and offset in recoil tuning, as well as the recoil  $\phi$  tuning parameters.

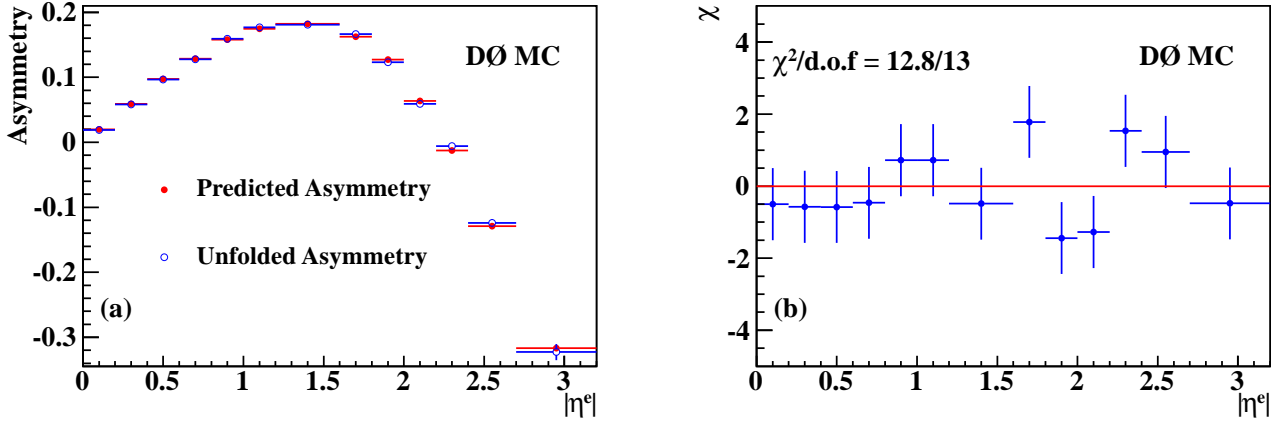


FIG. 10: (color online). (a) Closure test I of the unfolding method for the kinematic bin  $E_T^e > 25$  GeV,  $\cancel{E}_T > 25$  GeV, using half of the MC sample as input for the unfolding procedure and the other half as pseudo data. The solid red points are the PYTHIA generator-level electron asymmetries and the open blue points are the unfolded asymmetries. The asymmetries are shown after CP-folding. (b)  $\chi$  distribution between predicted asymmetry and unfolded asymmetry, where  $\chi_i = \Delta A_i / \sigma_i$ ,  $\Delta A_i$  is the difference between the generator-level asymmetry and the unfolded asymmetry, and  $\sigma_i$  is the statistical uncertainty in bin  $i$ .

TABLE II: Summary of absolute systematic uncertainties for the CP-folded electron charge asymmetry for kinematic bin  $E_T^e > 25$  GeV,  $\cancel{E}_T > 25$  GeV. The calorimeter has a gap in the range of  $1.1 < \eta_{\text{det}}^e < 1.5$ , so some systematic uncertainties in the  $\eta^e$  bin  $1.2 - 1.6$  are large compared to those of the neighboring  $\eta^e$  bins. The uncertainties are multiplied by 1000.

$\eta^e$	Gen	EMID	$K_{\text{eff}}^{q,p}$	Energy	Recoil	Model	Bkgs	$Q_{\text{mis}}$	Unfolding	Total
0.0 – 0.2	0.06	0.02	0.20	0.03	0.04	0.28	0.26	0.54	0.82	1.08
0.2 – 0.4	0.06	0.18	0.10	0.18	0.26	0.75	0.54	0.56	0.81	1.40
0.4 – 0.6	0.12	0.24	0.27	0.25	0.35	1.05	0.87	0.59	0.80	1.79
0.6 – 0.8	0.07	0.34	0.04	0.34	0.49	1.32	1.81	0.60	0.80	2.55
0.8 – 1.0	0.12	0.36	0.12	0.36	0.53	1.72	2.37	0.76	0.85	3.23
1.0 – 1.2	0.09	0.37	0.47	0.37	0.55	2.42	2.71	1.20	1.17	4.10
1.2 – 1.6	0.03	0.42	0.64	0.39	0.58	4.10	3.94	1.67	1.04	6.11
1.6 – 1.8	0.11	0.28	0.18	0.22	0.34	4.26	1.37	1.53	0.95	4.85
1.8 – 2.0	0.34	0.36	1.07	0.05	0.10	4.21	1.43	2.46	1.13	5.34
2.0 – 2.2	0.37	0.36	1.38	0.04	0.07	3.33	1.75	4.37	1.47	6.14
2.2 – 2.4	0.19	0.30	2.78	0.02	0.05	3.40	1.54	7.15	1.93	8.76
2.4 – 2.7	0.21	0.43	5.54	0.29	0.48	4.24	2.16	8.65	2.36	11.6
2.7 – 3.2	0.05	0.87	9.00	0.81	1.30	3.48	3.99	18.9	5.48	22.3

## F. Systematic uncertainty from MC modeling

The electron charge asymmetry measurement is determined from the numbers of electrons and positrons in each  $\eta^e$  bin. Thus, the differences in the distribution of kinematic quantities between data and MC will affect the measured asymmetry results. In order to minimize the effects from differences between data and MC, the MC sample is tuned to describe the data, but even after all of the corrections are applied, there are discrepancies in the high rapidity region, as shown in Fig. 12 for the  $E_T^e$  distribution with events in the  $-2.7$  to  $-2.4$   $\eta_{\text{det}}^e$  range. The MC may not be well modeled in some electron  $\eta^e$

bins, and we assign a systematic uncertainty to account for this.

To estimate the uncertainties from MC sample mis-modeling, we reweight the  $W^+$  and  $W^-$  events separately in each electron  $\eta^e$  bin, with the data/MC ratio (obtained separately for  $W^+$  and  $W^-$  events) as a function of  $M_T$ ,  $E_T^e$ , and  $\cancel{E}_T$ . The larger deviation between the samples with and without the reweighting factors in each bin is assigned as the symmetric systematic uncertainty in that bin. The uncertainties from  $M_T$ , electron  $E_T^e$ , and  $\cancel{E}_T$ , are combined in quadrature to arrive at a single total MC modeling uncertainty.

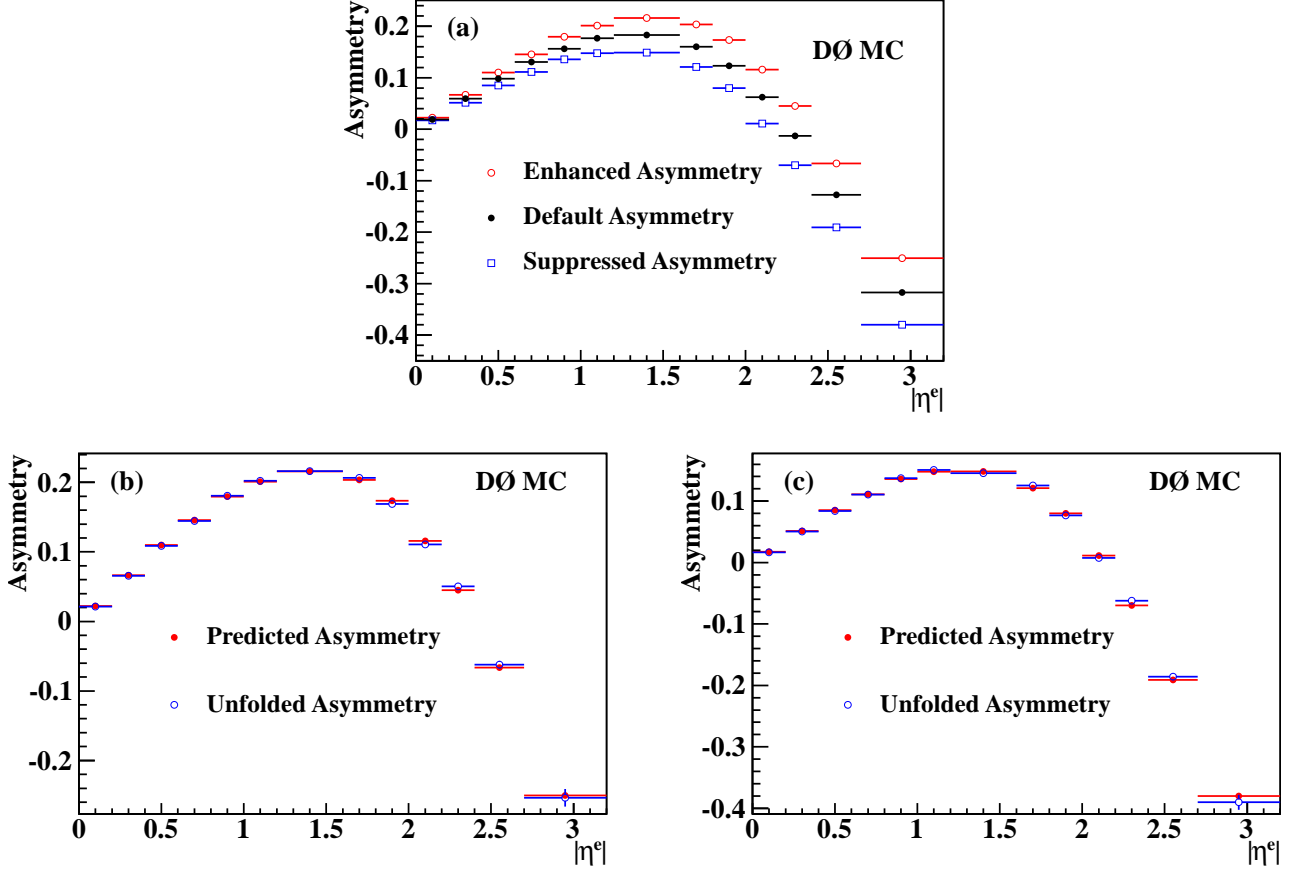


FIG. 11: (color online). (a) shows different input asymmetries used in the second closure test for the kinematic bin  $E_T^e > 25$  GeV,  $\cancel{E}_T > 25$  GeV. The solid black points represent the default asymmetry distribution generated using the PYTHIA generator with CTEQ6.1L PDFs, the open red points represent the enhanced input asymmetry, and the open blue squares point represent the suppressed input asymmetry. (b) and (c) show closure test II of the unfolding method using half of the MC sample as input for the unfolding procedure and the other half of the MC as pseudo data, where the generator-level asymmetries are enhanced or suppressed. A reweighting factor ( $f = 1 - 0.05 \times \eta^e$  for (b), and  $f = 1 + 0.05 \times \eta^e$  for (c)) has been applied to the number of electrons to ensure the generator-level asymmetries are far from the default values. The solid red points are generator-level electron asymmetries, the open blue points are the unfolded asymmetries. The asymmetries are shown after CP-folding.

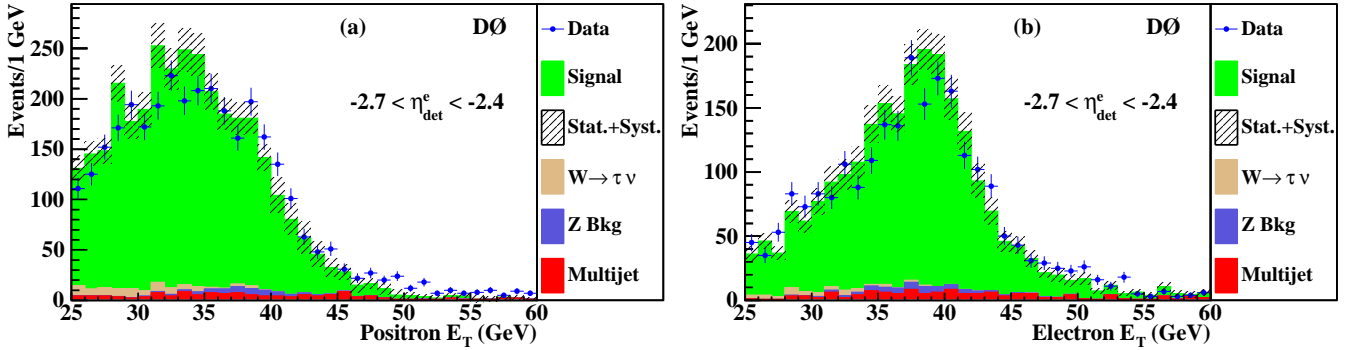


FIG. 12: (color online). Comparisons of the electron  $E_T$  distribution between data and the sum of signal and background predictions for selected (a)  $W^+$  and (b)  $W^-$  events in the range  $-2.7 < \eta_{\text{det}}^e < -2.4$ . This bin is chosen as the one showing the poorest agreement. In different rapidity regions, the values of  $x$  for  $u$  and  $d$  quarks are different, thus the  $W^+$  and  $W^-$  distributions are different from each other. The data uncertainty only represents the statistical uncertainty, and the bands represent the systematic uncertainty on the signal plus backgrounds, without any uncertainty from MC modelings.



TABLE III: Summary of absolute systematic uncertainties for the CP-folded electron charge asymmetry for kinematic bin  $25 < E_T^e < 35$  GeV,  $\cancel{E}_T > 25$  GeV. The calorimeter has a gap in the range of  $1.1 < \eta_{\text{det}}^e < 1.5$ , so some systematic uncertainties in the  $\eta^e$  bin  $1.2 - 1.6$  are large compared to those of the neighboring  $\eta^e$  bins. The uncertainties are multiplied by 1000.

$\eta^e$	Gen	EMID	$K_{\text{eff}}^{q,p}$	Energy	Recoil	Model	Bkgs	$Q_{\text{mis}}$	Unfolding	Total
0.0 – 0.2	0.10	0.01	0.10	0.03	0.02	0.07	0.11	1.99	1.27	2.37
0.2 – 0.4	0.19	0.25	0.11	0.54	0.39	0.11	0.39	1.93	1.25	2.45
0.4 – 0.6	0.54	0.39	0.27	0.80	0.56	0.28	0.55	2.10	1.25	2.80
0.6 – 0.8	0.52	0.50	0.12	1.03	0.70	0.43	1.02	1.80	1.25	2.85
0.8 – 1.0	0.56	0.50	0.17	0.90	0.75	0.22	1.47	1.79	1.33	3.03
1.0 – 1.2	0.53	0.50	0.34	0.74	0.78	0.56	1.88	2.50	1.88	3.93
1.2 – 1.6	0.52	0.35	0.42	0.35	0.27	0.97	2.09	2.32	1.74	3.81
1.6 – 1.8	0.41	0.20	0.06	0.65	0.35	1.43	1.00	2.35	1.59	3.44
1.8 – 2.0	0.71	0.72	0.39	1.07	0.86	2.72	0.72	3.82	1.90	5.40
2.0 – 2.2	0.95	0.89	0.58	1.60	1.34	2.79	1.38	6.29	2.44	7.85
2.2 – 2.4	0.77	0.83	0.86	2.05	1.28	1.97	1.68	9.20	3.06	10.4
2.4 – 2.7	0.47	1.25	2.64	2.25	1.68	2.08	4.66	10.3	3.40	12.7
2.7 – 3.2	0.38	1.91	14.2	3.18	2.97	4.46	5.75	20.8	7.14	27.5

TABLE IV: Summary of absolute systematic uncertainties for the CP-folded electron charge asymmetry for kinematic bin  $25 < E_T^e < 35$  GeV,  $25 < \cancel{E}_T < 35$  GeV. The calorimeter has a gap in the range of  $1.1 < \eta_{\text{det}}^e < 1.5$ , so some systematic uncertainties in the  $\eta^e$  bin  $1.2 - 1.6$  are large compared to those of the neighboring  $\eta^e$  bins. The uncertainties are multiplied by 1000.

$\eta^e$	Gen	EMID	$K_{\text{eff}}^{q,p}$	Energy	Recoil	Model	Bkgs	$Q_{\text{mis}}$	Unfolding	Total
0.0 – 0.2	0.06	0.08	0.10	0.13	0.17	0.34	0.08	1.99	1.77	2.70
0.2 – 0.4	0.37	0.27	0.10	0.39	0.53	0.66	0.34	1.93	1.74	2.82
0.4 – 0.6	0.52	0.47	0.33	0.61	0.76	0.86	0.38	2.10	1.73	3.14
0.6 – 0.8	0.39	0.51	0.13	0.68	0.91	1.23	0.60	1.80	1.74	3.14
0.8 – 1.0	0.44	0.48	0.25	0.62	0.95	1.10	1.03	1.79	1.87	3.28
1.0 – 1.2	0.31	0.37	0.27	0.47	0.89	1.60	1.38	2.50	2.70	4.40
1.2 – 1.6	0.11	0.32	0.37	0.36	0.59	1.95	1.97	2.32	2.52	4.48
1.6 – 1.8	0.68	0.84	0.10	0.87	1.14	1.28	1.07	2.35	2.24	4.07
1.8 – 2.0	0.97	1.68	0.54	1.78	2.38	2.59	1.33	3.82	2.69	6.57
2.0 – 2.2	1.23	1.88	0.61	2.04	3.34	3.77	2.34	6.29	3.42	9.58
2.2 – 2.4	0.39	1.35	0.92	1.96	2.84	3.36	2.83	9.20	4.16	11.7
2.4 – 2.7	0.27	1.63	1.99	2.39	3.43	6.38	6.13	10.3	4.43	15.1
2.7 – 3.2	0.35	2.19	13.7	3.34	4.81	9.76	5.37	20.8	8.98	29.4

### G. Systematic uncertainty from background modeling

The statistical uncertainties in the background MC samples and the uncertainty in the integrated luminosity measurement contribute to the overall asymmetry systematic uncertainty. For the  $Z \rightarrow ee$ ,  $Z \rightarrow \tau\tau$ , and  $W \rightarrow \tau\nu$  backgrounds using NLO cross sections, we vary the integrated luminosity by  $\pm 6.1\%$  [17], extract the asymmetries with the varied integrated luminosity, and take the larger variation as the systematic uncertainty due to the luminosity. To study systematic uncertainties

from the multijet  $M_T$  shape, we vary the reversed shower shape cuts, extract the asymmetries with the different multijet  $M_T$  shapes, and take the larger variation as the systematic uncertainty. Similarly for the systematic uncertainty in the multijet fraction, we vary the multijet scale factors in the template fitting by  $\pm 1$  standard deviation, extract the asymmetries with the different multijet contributions, and take the larger variation in each bin as a symmetric systematic uncertainty in that bin. The uncertainties from luminosity and multijet background are combined in quadrature to arrive at a single total background modeling uncertainty.

TABLE V: Summary of absolute systematic uncertainties for the CP-folded electron charge asymmetry for kinematic bin  $E_T^e > 35$  GeV,  $\cancel{E}_T > 25$  GeV. The calorimeter has a gap in the range of  $1.1 < \eta_{\text{det}}^e < 1.5$ , so some systematic uncertainties in the  $\eta^e$  bin  $1.2 - 1.6$  are large compared to those of the neighboring  $\eta^e$  bins. The uncertainties are multiplied by 1000.

$\eta^e$	Gen	EMID	$K_{\text{eff}}^{q,p}$	Energy	Recoil	Model	Bkgs	$Q_{\text{mis}}$	Unfolding	Total
0.0 – 0.2	0.04	0.03	0.26	0.04	0.06	0.37	0.31	0.48	1.06	1.29
0.2 – 0.4	0.04	0.16	0.12	0.24	0.23	1.14	0.53	0.54	1.04	1.77
0.4 – 0.6	0.20	0.18	0.25	0.30	0.26	1.89	0.95	0.58	1.03	2.48
0.6 – 0.8	0.28	0.29	0.31	0.46	0.42	2.27	2.20	0.63	1.02	3.47
0.8 – 1.0	0.26	0.35	0.39	0.52	0.51	2.72	2.82	0.82	1.07	4.25
1.0 – 1.2	0.56	0.39	0.77	0.52	0.56	3.76	3.11	1.34	1.47	5.42
1.2 – 1.6	0.47	0.60	1.34	0.69	0.80	6.22	5.47	2.16	1.28	8.86
1.6 – 1.8	0.46	0.58	0.84	0.72	0.79	6.31	3.22	1.93	1.16	7.60
1.8 – 2.0	0.65	0.86	1.64	0.70	0.76	6.29	1.65	3.15	1.36	7.68
2.0 – 2.2	0.70	0.73	1.88	0.61	0.51	5.54	3.19	5.92	1.77	9.18
2.2 – 2.4	0.68	0.38	3.20	0.69	0.35	5.28	4.31	10.6	2.37	13.3
2.4 – 2.7	0.46	0.71	5.23	0.90	0.72	5.32	2.47	14.6	3.05	16.9
2.7 – 3.2	1.43	0.31	14.8	0.87	0.32	8.99	3.48	35.0	7.94	40.0

TABLE VI: Summary of absolute systematic uncertainties for the CP-folded electron charge asymmetry for kinematic bin  $E_T^e > 35$  GeV,  $\cancel{E}_T > 35$  GeV. The calorimeter has a gap in the range of  $1.1 < \eta_{\text{det}}^e < 1.5$ , so some systematic uncertainties in the  $\eta^e$  bin  $1.2 - 1.6$  are large compared to those of the neighboring  $\eta^e$  bins. The uncertainties are multiplied by 1000.

$\eta^e$	Gen	EMID	$K_{\text{eff}}^{q,p}$	Energy	Recoil	Model	Bkgs	$Q_{\text{mis}}$	Unfolding	Total
0.0 – 0.2	0.06	0.00	0.25	0.03	0.08	0.18	0.10	0.48	1.30	1.42
0.2 – 0.4	0.05	0.04	0.12	0.07	0.16	0.59	0.17	0.54	1.27	1.53
0.4 – 0.6	0.06	0.06	0.23	0.09	0.19	1.09	0.26	0.58	1.26	1.81
0.6 – 0.8	0.03	0.14	0.32	0.22	0.33	1.52	0.50	0.63	1.25	2.19
0.8 – 1.0	0.10	0.20	0.41	0.29	0.45	2.11	0.70	0.82	1.32	2.81
1.0 – 1.2	0.08	0.27	0.77	0.34	0.73	2.30	0.92	1.34	1.83	3.55
1.2 – 1.6	0.24	0.40	1.32	0.44	0.73	3.88	1.98	2.16	1.59	5.37
1.6 – 1.8	0.57	0.44	0.89	0.44	0.85	3.97	0.94	1.93	1.40	4.95
1.8 – 2.0	0.65	0.65	1.66	0.48	0.93	3.00	0.75	3.15	1.64	5.18
2.0 – 2.2	1.01	0.61	1.87	0.30	0.85	2.76	1.22	5.92	2.13	7.37
2.2 – 2.4	1.71	0.35	3.27	0.47	1.00	2.99	2.07	10.6	2.83	12.2
2.4 – 2.7	2.70	0.76	5.01	0.48	1.09	1.27	3.21	14.6	3.67	16.5
2.7 – 3.2	3.18	0.41	16.8	0.62	0.71	3.17	3.12	35.0	9.90	40.4

#### H. Systematic uncertainty from the electron charge misidentification

We vary the charge misidentification probability ( $Q_{\text{mis}}$ ) in data by  $\pm 1$  standard deviation, extract the asymmetries with the varied charge misidentification, and take the larger variation in each bin as a symmetric systematic uncertainty in that bin.

#### I. Systematic uncertainty from the unfolding procedure

To determine the systematic uncertainty due to the limited statistics used in the calculation of the migration matrices, we divide the MC sample into ten sub-samples and perform ten pseudo-experiments. The root mean squared spread of the ten unfolded asymmetry distributions is divided by  $\sqrt{10}$  for each bin, and this is taken as the systematic uncertainty.

An uncertainty on the  $\mathcal{A} \times \epsilon$  corrections arises from the statistics of the  $W$  boson MC samples. This uncertainty is determined when we study the  $\mathcal{A} \times \epsilon$  correc-

tions ( $A^{\text{Gen}} - A^{\text{Reco}}$ ) by varying the  $\mathcal{A} \times \epsilon$  corrections by  $\pm 1$  standard deviation and using the larger variation of asymmetry in each bin as a symmetric systematic uncertainty in that bin.

The uncertainties from migration matrices and  $\mathcal{A} \times \epsilon$  are combined in quadrature to arrive at a single total unfolding procedure uncertainty.

## J. Correlations between systematic uncertainties

The electron charge asymmetries are measured in different  $\eta^e$  bins. In the estimation of systematic uncertainties, the migrations introduce correlations between different  $\eta^e$  bins. To estimate the correlations of the systematic uncertainties between different  $\eta^e$  bins, we study each systematic uncertainty individually, and after determining the correlations as explained next, we build the correlation matrix in each  $\eta^e$  bin for the various systematic uncertainties.

The systematic uncertainties from the generator level, which include  $W$  boson  $p_T$  and FSR modeling, shift the electron charge asymmetry in all of the  $\eta^e$  bins simultaneously. We therefore assume this correlation in the asymmetry measurement is 100%. Similarly, for the electron energy tuning, recoil modeling, MC modeling, background modeling, and unfolding procedure, 100% correlation between each  $\eta^e$  bin is assumed when producing the correlation matrix. The other systematic uncertainties, e.g., EMID and electron charge misidentification, are obtained using  $Z \rightarrow ee$  events with the same bin size as the electron asymmetry measurement. We therefore assume there is zero correlation between  $\eta^e$  bins. With the assumptions described above and combined in quadrature, we build the correlation matrices for each kinematic bin, which are presented in Tables VII–XI.

## VIII. RESULTS

The asymmetry results for  $\eta^e > 0$  are found to be consistent with those for  $\eta^e < 0$ , so we assume CP invariance with  $A(\eta^e)$  being equivalent to  $-A(-\eta^e)$ . The data for  $\eta^e < 0$  are folded appropriately with those for  $\eta^e > 0$  to increase the statistics, and results are presented for  $|\eta^e|$ . We perform the electron charge asymmetry measurement in five kinematic bins. Results from the different kinematic bins probe different ranges of  $y_W$ , and thus different ranges of the fraction of proton momentum carried by the parton. The measured electron asymmetries with symmetric kinematic cuts on  $E_T^e$  and  $\cancel{E}_T$  ( $E_T^e > 25$  GeV,  $\cancel{E}_T > 25$  GeV;  $25 < E_T^e < 35$  GeV,  $25 < \cancel{E}_T < 35$  GeV; and  $E_T^e > 35$  GeV,  $\cancel{E}_T > 35$  GeV) and the differences between measured values and MC@NLO [34] with the NNPDF2.3 [35] PDF set predictions are shown in Figs. 13–15. For the measured electron asymmetries with asymmetric kinematic cuts ( $25 < E_T^e < 35$  GeV,  $\cancel{E}_T > 25$  GeV;  $E_T^e > 35$  GeV,  $\cancel{E}_T > 25$  GeV), the differ-

ences between measured values and predictions are shown in Figs. 16 and 17. The PDF bands are obtained from MC@NLO using the NNPDF2.3 NLO PDF uncertainty sets. The central value of predictions from MC@NLO with HERWIG [36] using the MSTW2008NLO [37] central PDF set and from RESBOS with PHOTOS [25] (for QED final state radiation) using the CTEQ6.6 central PDF set are also included. The theory curves are generated with selection criteria applied to the electron and neutrino generator-level transverse momenta, with all the radiated photons merged into the electron if they fall within a cone of radius  $\Delta R < 0.3$ . Generator-level  $W$  bosons are further required to have a transverse mass in the range between 50 and 200 GeV and to have a transverse momentum less than 120 GeV.

The measured electron charge asymmetries are consistent with predictions for the inclusive kinematic bin  $E_T^e > 25$  GeV,  $\cancel{E}_T > 25$  GeV. In the kinematic bins with asymmetric cuts ( $25 < E_T^e < 35$  GeV,  $\cancel{E}_T > 25$  GeV;  $E_T^e > 35$  GeV,  $\cancel{E}_T > 25$  GeV), the measured electron charge asymmetries are consistent with predictions from RESBOS using the CTEQ6.6 central PDF set, but in the kinematic bins with symmetric cuts ( $25 < E_T^e < 35$  GeV,  $25 < \cancel{E}_T < 35$  GeV;  $E_T^e > 35$  GeV,  $\cancel{E}_T > 35$  GeV), the measured electron charge asymmetries are not consistent with any of the considered predictions, with the  $\chi^2/d.o.f.$  between measured asymmetry and the MC@NLO with NNPDF2.3 predictions equal to 47.1/13 and 95.5/13, respectively. The results presented here are in good agreement with those of Ref. [12] for the muon charge asymmetry for both  $E_T^\ell > 25$  GeV,  $\cancel{E}_T > 25$  GeV and  $E_T^\ell > 35$  GeV,  $\cancel{E}_T > 35$  GeV. This agreement is noteworthy since the analysis techniques and dominant systematic uncertainties in the two measurements are quite different. The results are consistent with the previously published results [11] in the  $|\eta^e| < 2$  region, and disagree in the high  $|\eta^e|$  region. In this paper, compared to the previous results [11], there are several improvements for the modeling of electrons in high  $|\eta^e|$  region, including the  $\eta$ -dependent energy scale corrections, recoil system modeling, and the positron/electron identification efficiency corrections. This measurement thus supersedes the results of Ref. [11].

The electron charge asymmetry measurements for various bins in  $\eta^e$  for the five kinematic regions, and their uncertainties together with MC@NLO predictions using the NNPDF2.3 PDF sets are listed in Tables XII–XIV. In most  $\eta^e$  bins and kinematic bins, the experimental uncertainties are smaller than the uncertainties from the predictions, especially in the high  $\eta^e$  region, demonstrating the importance of this analysis for improving the accuracy of future PDF fits.

To estimate the correlation between the measured asymmetry within different kinematic bins as a function of  $\eta^e$  bin, we use the numbers of selected electrons and positrons in data and the migration matrices and acceptances obtained from  $W \rightarrow e\nu$  MC to study the statistical correlations between kinematic bins. The correlation

TABLE VII: Correlation matrix of the systematic uncertainties between different  $|\eta^e|$  bins for events with  $E_T^e > 25$  GeV,  $\cancel{E}_T > 25$  GeV. The “ $|\eta^e|$  bin” represents the indexing of the  $\eta^e$  bins used in this analysis.

$ \eta^e $ bin	1	2	3	4	5	6	7	8	9	10	11	12	13
1	1.00	0.83	0.79	0.74	0.72	0.73	0.68	0.67	0.66	0.63	0.56	0.55	0.52
2		1.00	0.90	0.89	0.87	0.88	0.85	0.84	0.81	0.74	0.64	0.63	0.56
3			1.00	0.92	0.92	0.92	0.90	0.87	0.84	0.76	0.65	0.64	0.55
4				1.00	0.96	0.95	0.94	0.86	0.82	0.75	0.63	0.63	0.55
5					1.00	0.95	0.95	0.86	0.82	0.75	0.63	0.63	0.54
6						1.00	0.94	0.88	0.84	0.76	0.64	0.64	0.54
7							1.00	0.90	0.86	0.77	0.64	0.64	0.52
8								1.00	0.90	0.78	0.66	0.65	0.49
9									1.00	0.75	0.63	0.62	0.47
10										1.00	0.56	0.55	0.44
11											1.00	0.47	0.38
12												1.00	0.38
13													1.00

TABLE VIII: Correlation matrix of the systematic uncertainties between different  $|\eta^e|$  bins for events with  $25 < E_T^e < 35$  GeV,  $\cancel{E}_T > 25$  GeV.

$ \eta^e $ bin	1	2	3	4	5	6	7	8	9	10	11	12	13
1	1.00	0.54	0.51	0.52	0.53	0.54	0.53	0.53	0.47	0.44	0.42	0.41	0.40
2		1.00	0.61	0.65	0.65	0.64	0.61	0.61	0.55	0.53	0.50	0.52	0.46
3			1.00	0.69	0.69	0.66	0.63	0.63	0.59	0.57	0.53	0.54	0.48
4				1.00	0.76	0.74	0.72	0.70	0.64	0.63	0.57	0.62	0.53
5					1.00	0.76	0.75	0.69	0.62	0.61	0.57	0.63	0.54
6						1.00	0.75	0.70	0.63	0.61	0.56	0.63	0.54
7							1.00	0.72	0.64	0.61	0.55	0.63	0.54
8								1.00	0.69	0.64	0.56	0.59	0.53
9									1.00	0.63	0.54	0.54	0.49
10										1.00	0.51	0.52	0.47
11											1.00	0.47	0.42
12												1.00	0.46
13													1.00

matrix is defined as  $c_{ij}/\sqrt{c_{ii}c_{jj}}$ , where  $c_{ij}$  represents the element of the statistical covariance matrix between  $\eta^e$  bins  $i$  and  $j$  calculated by summing partial derivatives of the asymmetry,

$$c_{ij} = \sum_f \sum_k \frac{\partial A_i}{\partial f_k} \cdot \frac{\partial A_j}{\partial f_k} \cdot (\Delta f_k)^2 \quad (9)$$

where  $k$  represents the number of  $\eta^e$  bins,  $f$  represents the sources of uncertainty from each non-overlapping kinematic bin, and  $A_i$  is the measured asymmetry in  $\eta^e$  bin  $i$ . The correlation matrices between central values in each  $\eta^e$  bin for the five kinematic bins after CP folding are given in Tables XV–XIX. From these tables, we can see that the off-diagonal elements of the statistical correlation matrices are small, which indicates the migration effects are small between different  $\eta^e$  bins. The statisti-

cal uncertainties in Tables XII–XIV are calculated using the covariance matrix, with  $\sigma_i = \sqrt{c_{ii}}$ .

Besides small migration between  $\eta^e$  bins, there are significant migration effects between kinematic bins, due to detector resolution effects. In Table XX we show the fraction of MC signal events originating in a different generator-level kinematic bin that are found in a given reconstruction-level bin. The categories in Table XX are not independent. In Table XX,  $20 < p_T^e < 25$  OR  $20 < p_T^\nu < 25$  GeV denotes  $W$  boson events in which either the electron  $p_T^e$  at the generator level ( $E_T^e$  at the reconstruction level) is in the range 20 to 25 GeV or the neutrino  $p_T^\nu$  ( $\cancel{E}_T$ ) is in the range 20 to 25 GeV, while the other lepton  $p_T$  ( $E_T$ ) is above 25 GeV. Also  $p_T^e > 25$  AND  $p_T^\nu > 25$  GeV denotes  $W$  boson events in which the electron  $p_T^e$  ( $E_T^e$ ) is above 25 GeV and the neutrino  $p_T^\nu$  ( $\cancel{E}_T$ ) is above 25 GeV.

TABLE IX: Correlation matrix of the systematic uncertainties between different  $|\eta^e|$  bins for events with  $25 < E_T^e < 35$  GeV,  $25 < \cancel{E}_T < 35$  GeV.

$ \eta^e $ bin	1	2	3	4	5	6	7	8	9	10	11	12	13
1	1.00	0.68	0.65	0.67	0.68	0.69	0.67	0.66	0.60	0.57	0.55	0.53	0.51
2		1.00	0.72	0.75	0.75	0.75	0.73	0.74	0.70	0.67	0.62	0.63	0.58
3			1.00	0.75	0.76	0.75	0.73	0.75	0.72	0.69	0.63	0.64	0.59
4				1.00	0.81	0.80	0.79	0.79	0.78	0.75	0.68	0.71	0.64
5					1.00	0.81	0.81	0.80	0.78	0.76	0.70	0.73	0.64
6						1.00	0.82	0.79	0.76	0.74	0.69	0.73	0.64
7							1.00	0.79	0.75	0.74	0.69	0.75	0.65
8								1.00	0.77	0.74	0.68	0.71	0.63
9									1.00	0.74	0.67	0.70	0.62
10										1.00	0.65	0.70	0.61
11											1.00	0.64	0.56
12												1.00	0.60
13													1.00

TABLE X: Correlation matrix of the systematic uncertainties between different  $|\eta^e|$  bins for events with  $E_T^e > 35$  GeV,  $\cancel{E}_T > 25$  GeV.

$ \eta^e $ bin	1	2	3	4	5	6	7	8	9	10	11	12	13
1	1.00	0.87	0.81	0.77	0.75	0.75	0.69	0.69	0.66	0.65	0.58	0.53	0.50
2		1.00	0.94	0.91	0.89	0.90	0.87	0.88	0.85	0.79	0.69	0.61	0.54
3			1.00	0.95	0.94	0.94	0.92	0.94	0.90	0.83	0.72	0.62	0.54
4				1.00	0.97	0.96	0.96	0.94	0.87	0.83	0.73	0.60	0.52
5					1.00	0.96	0.96	0.94	0.86	0.83	0.73	0.60	0.51
6						1.00	0.95	0.94	0.88	0.83	0.72	0.60	0.52
7							1.00	0.94	0.87	0.83	0.72	0.59	0.49
8								1.00	0.91	0.83	0.71	0.60	0.51
9									1.00	0.79	0.66	0.58	0.49
10										1.00	0.63	0.53	0.46
11											1.00	0.46	0.40
12												1.00	0.35
13													1.00

## IX. CONCLUSIONS

In summary, we have measured the electron charge asymmetry in  $p\bar{p} \rightarrow W^\pm + X \rightarrow e^\pm \nu + X$  events using  $9.7 \text{ fb}^{-1}$  of integrated luminosity collected by the D0 experiment in  $p\bar{p}$  collisions at  $\sqrt{s} = 1.96 \text{ TeV}$ . In this analysis, the electron pseudorapidity coverage is extended to  $|\eta^e| = 3.2$  and is thus sensitive to  $W$  bosons created by small- and large- $x$  partons. Our measurement is the most precise lepton charge asymmetry measurement to date. The uncertainty on the measured asymmetry is smaller than the PDF uncertainty for most of the bins. We provide the correlation coefficients for different  $|\eta^e|$  bins and the correlation coefficients between different kinematic bins, to be used for future PDF determinations.

This measurement supersedes the results of Ref. [11].

It also complements and provides more details on the results of Ref. [14] which measured the  $W^\pm$  boson charge asymmetry using the same data set. These asymmetries are in good agreement with those measured in the muon decay channel [12]. The electron asymmetries presented here include the effects of the  $W$  boson decay asymmetry, whereas the Ref. [14] analysis solely addresses the production asymmetry. Both measurements should be useful in future analyses of the PDFs.

We thank the staffs at Fermilab and collaborating institutions, and acknowledge support from the Department of Energy and National Science Foundation (United States of America); Alternative Energies and Atomic Energy Commission and National Center for Scientific Research/National Institute of Nuclear and Particle Physics (France); Ministry of Education and Science of the Russian Federation, National Research Center ‘‘Kurchatov

TABLE XI: Correlation matrix of the systematic uncertainties between different  $|\eta^e|$  bins for events with  $E_T^e > 35$  GeV,  $\cancel{E}_T > 35$  GeV.

$ \eta^e $ bin	1	2	3	4	5	6	7	8	9	10	11	12	13
1	1.00	0.91	0.85	0.80	0.74	0.76	0.63	0.62	0.62	0.58	0.51	0.49	0.49
2		1.00	0.92	0.89	0.86	0.86	0.76	0.77	0.73	0.65	0.57	0.50	0.50
3			1.00	0.93	0.92	0.90	0.84	0.86	0.79	0.68	0.59	0.49	0.48
4				1.00	0.94	0.92	0.88	0.89	0.81	0.70	0.60	0.49	0.47
5					1.00	0.92	0.90	0.91	0.81	0.70	0.60	0.48	0.45
6						1.00	0.87	0.87	0.79	0.68	0.59	0.48	0.45
7							1.00	0.88	0.78	0.66	0.57	0.46	0.41
8								1.00	0.80	0.67	0.57	0.44	0.40
9									1.00	0.61	0.52	0.42	0.39
10										1.00	0.47	0.40	0.36
11											1.00	0.36	0.32
12												1.00	0.30
13													1.00

TABLE XII: CP-folded electron charge asymmetry for data and predictions from MC@NLO using NNPDF2.3 PDFs multiplied by 100.  $\langle|\eta^e|\rangle$  is the cross section weighted average of electron pseudorapidity in each bin from RESBOS with PHOTOS. For data, the first uncertainty is statistical and the second is systematic. The uncertainties on the prediction are due to uncertainties on the PDFs.

$\langle \eta^e \rangle$	$E_T^e > 25$ GeV $\cancel{E}_T > 25$ GeV	
	Data	Prediction
0.10	$2.10 \pm 0.12 \pm 0.11$	$1.90 \pm 0.16$
0.30	$5.23 \pm 0.11 \pm 0.14$	$5.55 \pm 0.31$
0.50	$9.16 \pm 0.11 \pm 0.18$	$8.93 \pm 0.44$
0.70	$11.97 \pm 0.11 \pm 0.25$	$12.04 \pm 0.54$
0.90	$14.52 \pm 0.12 \pm 0.32$	$14.50 \pm 0.60$
1.10	$15.59 \pm 0.18 \pm 0.41$	$15.74 \pm 0.66$
1.39	$15.37 \pm 0.67 \pm 0.61$	$15.41 \pm 0.70$
1.70	$11.05 \pm 0.31 \pm 0.49$	$11.50 \pm 0.83$
1.90	$6.66 \pm 1.19 \pm 0.53$	$5.84 \pm 0.92$
2.10	$-1.55 \pm 0.53 \pm 0.61$	$-1.68 \pm 1.03$
2.30	$-9.97 \pm 0.71 \pm 0.88$	$-11.00 \pm 1.17$
2.54	$-19.10 \pm 0.41 \pm 1.16$	$-24.05 \pm 1.38$
2.92	$-39.97 \pm 0.93 \pm 2.23$	$-43.73 \pm 1.94$

Institute” of the Russian Federation, and Russian Foundation for Basic Research (Russia); National Council for the Development of Science and Technology and Carlos Chagas Filho Foundation for the Support of Research in the State of Rio de Janeiro (Brazil); Department of Atomic Energy and Department of Science and Technology (India); Administrative Department of Science, Technology and Innovation (Colombia); National Council of Science and Technology (Mexico); National Research Foundation of Korea (Korea); Foundation for Fundamental Research on Matter (The Netherlands); Science and Technology Facilities Council and The Royal Society (United Kingdom); Ministry of Education, Youth and Sports (Czech Republic); Bundesministerium für Bildung und Forschung (Federal Ministry of Education and Research) and Deutsche Forschungsgemeinschaft (German Research Foundation) (Germany); Science Foundation Ireland (Ireland); Swedish Research Council (Sweden); China Academy of Sciences and National Natural Science Foundation of China (China); and Ministry of Education and Science of Ukraine (Ukraine).

- [1] E. L. Berger, F. Halzen, C. S. Kim and S. Willenbrock, Phys. Rev. D **40**, 83 (1989).
- [2] A. D. Martin, R. G. Roberts, and W. J. Stirling, Mod. Phys. Lett. A **4**, 1135 (1989).
- [3] H. L. Lai *et al.*, Phys. Rev. D **51**, 4763 (1995).
- [4] D0 uses a cylindrical coordinate system with the  $z$  axis along the beam axis in the proton direction. Angles  $\theta$

- and  $\phi$  are the polar and azimuthal angles, respectively. Pseudorapidity is defined as  $\eta = -\ln[\tan(\theta/2)]$ , where  $\theta$  is measured with respect to the  $p\bar{p}$  interaction vertex. In the massless limit,  $\eta$  is equivalent to the rapidity  $y = (1/2) \ln[(E + p_z)/(E - p_z)]$ .  $\eta_{\text{det}}$  is the pseudorapidity measured with respect to the center of the detector.
- [5] C. Balazs and C. P. Yuan, Phys. Rev. D **56**, 5558 (1997).

TABLE XIII: CP-folded electron charge asymmetry for data and predictions from MC@NLO using NNPDF2.3 PDFs multiplied by 100.  $\langle|\eta^e|\rangle$  is the cross section weighted average of electron pseudorapidity in each bin from RESBOS with PHOTOS. For data, the first uncertainty is statistical and the second is systematic. The uncertainties on the prediction are due to uncertainties on the PDFs.

$\langle \eta^e \rangle$	$25 < E_T^e < 35 \text{ GeV}$		$25 < E_T^e < 35 \text{ GeV}$	
	$\cancel{E}_T > 25 \text{ GeV}$		$25 < \cancel{E}_T < 35 \text{ GeV}$	
	Data	Prediction	Data	Prediction
0.10	$2.32 \pm 0.16 \pm 0.24$	$2.47 \pm 0.21$	$2.30 \pm 0.19 \pm 0.27$	$2.07 \pm 0.24$
0.30	$6.36 \pm 0.15 \pm 0.24$	$7.18 \pm 0.38$	$6.93 \pm 0.18 \pm 0.28$	$6.04 \pm 0.51$
0.50	$10.53 \pm 0.15 \pm 0.27$	$11.26 \pm 0.60$	$11.31 \pm 0.17 \pm 0.31$	$9.00 \pm 0.78$
0.70	$12.60 \pm 0.14 \pm 0.28$	$14.73 \pm 0.73$	$12.97 \pm 0.17 \pm 0.31$	$11.55 \pm 0.98$
0.90	$14.58 \pm 0.16 \pm 0.30$	$17.10 \pm 0.80$	$14.92 \pm 0.18 \pm 0.32$	$12.44 \pm 1.02$
1.10	$14.11 \pm 0.23 \pm 0.39$	$17.36 \pm 0.87$	$13.85 \pm 0.27 \pm 0.44$	$10.98 \pm 1.14$
1.39	$9.95 \pm 0.74 \pm 0.38$	$13.74 \pm 0.87$	$6.63 \pm 0.88 \pm 0.45$	$3.78 \pm 1.17$
1.70	$-1.40 \pm 0.44 \pm 0.34$	$3.24 \pm 0.94$	$-7.99 \pm 0.51 \pm 0.40$	$-12.19 \pm 1.24$
1.90	$-12.70 \pm 1.72 \pm 0.54$	$-8.31 \pm 0.98$	$-21.85 \pm 1.70 \pm 0.65$	$-27.66 \pm 1.23$
2.10	$-28.36 \pm 0.76 \pm 0.78$	$-21.63 \pm 1.09$	$-40.05 \pm 0.85 \pm 0.95$	$-42.94 \pm 1.28$
2.30	$-41.27 \pm 0.93 \pm 1.04$	$-33.54 \pm 1.15$	$-52.93 \pm 1.00 \pm 1.17$	$-53.65 \pm 1.27$
2.54	$-50.86 \pm 0.48 \pm 1.26$	$-44.33 \pm 1.32$	$-59.43 \pm 0.49 \pm 1.51$	$-61.49 \pm 1.38$
2.92	$-60.00 \pm 1.04 \pm 2.75$	$-55.99 \pm 2.05$	$-64.68 \pm 1.07 \pm 2.94$	$-69.79 \pm 2.13$

TABLE XIV: CP-folded electron charge asymmetry for data and predictions from MC@NLO using NNPDF2.3 PDFs multiplied by 100.  $\langle|\eta^e|\rangle$  is the cross section weighted average of electron pseudorapidity in each bin from RESBOS with PHOTOS. For data, the first uncertainty is statistical and the second is systematic. The uncertainties on the prediction are due to uncertainties on the PDFs.

$\langle \eta^e \rangle$	$E_T^e > 35 \text{ GeV}$		$E_T^e > 35 \text{ GeV}$	
	$\cancel{E}_T > 25 \text{ GeV}$		$\cancel{E}_T > 35 \text{ GeV}$	
	Data	Prediction	Data	Prediction
0.10	$1.94 \pm 0.14 \pm 0.13$	$1.47 \pm 0.28$	$1.65 \pm 0.16 \pm 0.14$	$1.70 \pm 0.32$
0.30	$4.26 \pm 0.14 \pm 0.18$	$4.33 \pm 0.35$	$3.78 \pm 0.15 \pm 0.15$	$5.25 \pm 0.42$
0.50	$8.04 \pm 0.13 \pm 0.25$	$7.22 \pm 0.39$	$6.89 \pm 0.15 \pm 0.18$	$8.67 \pm 0.39$
0.70	$11.42 \pm 0.13 \pm 0.35$	$10.06 \pm 0.55$	$9.94 \pm 0.15 \pm 0.22$	$12.15 \pm 0.56$
0.90	$14.40 \pm 0.14 \pm 0.42$	$12.62 \pm 0.60$	$12.61 \pm 0.16 \pm 0.28$	$15.47 \pm 0.59$
1.10	$16.63 \pm 0.21 \pm 0.54$	$14.60 \pm 0.68$	$15.02 \pm 0.23 \pm 0.35$	$18.05 \pm 0.69$
1.39	$18.95 \pm 0.76 \pm 0.88$	$16.53 \pm 0.75$	$18.25 \pm 0.69 \pm 0.54$	$21.34 \pm 0.77$
1.70	$19.07 \pm 0.36 \pm 0.76$	$16.80 \pm 0.91$	$19.66 \pm 0.40 \pm 0.49$	$23.33 \pm 0.94$
1.90	$18.98 \pm 1.38 \pm 0.77$	$14.86 \pm 1.00$	$21.06 \pm 1.33 \pm 0.51$	$23.10 \pm 1.00$
2.10	$15.61 \pm 0.61 \pm 0.92$	$11.68 \pm 1.16$	$19.50 \pm 0.68 \pm 0.73$	$22.15 \pm 1.20$
2.30	$11.89 \pm 0.85 \pm 1.33$	$6.43 \pm 1.34$	$18.08 \pm 0.93 \pm 1.21$	$19.65 \pm 1.35$
2.54	$9.14 \pm 0.51 \pm 1.69$	$-2.63 \pm 1.76$	$17.58 \pm 0.58 \pm 1.63$	$14.16 \pm 1.77$
2.92	$-1.93 \pm 1.32 \pm 4.00$	$-17.68 \pm 3.04$	$11.07 \pm 1.56 \pm 4.03$	$4.13 \pm 3.51$

- [6] P. M. Nadolsky, H.-L. Lai, Q.-H. Cao, J. Huston, J. Pumplin, D. Stump, W.-K. Tung, and C.-P. Yuan, Phys. Rev. D **78**, 013004 (2008).  
[7] F. Abe *et al.* (CDF Collaboration), Phys. Rev. Lett. **74**, 850 (1995).  
[8] F. Abe *et al.* (CDF Collaboration), Phys. Rev. Lett. **81**, 5754 (1998).  
[9] D. Acosta *et al.* (CDF Collaboration), Phys. Rev. D **71**, 051104 (2005).  
[10] V. M. Abazov *et al.* (D0 Collaboration), Phys. Rev. D **77**, 011106 (2008).  
[11] V. M. Abazov *et al.* (D0 Collaboration), Phys. Rev. Lett. **101**, 211801 (2008).  
[12] V. M. Abazov *et al.* (D0 Collaboration), Phys. Rev. D **88**, 091102(R) (2013).  
[13] T. Aaltonen *et al.* (CDF Collaboration), Phys. Rev. Lett.



- 102**, 181801 (2009).
- [14] V. M. Abazov *et al.* (D0 Collaboration), Phys. Rev. Lett **112**, 151803 (2014).
  - [15] G. Aad *et al.* (ATLAS Collaboration), Phys. Rev. D **85**, 072004 (2012).
  - [16] S. Chatrchyan *et al.* (CMS Collaboration), J. High Energy Phys. **04**, 050 (2011).
  - [17] T. Andeen *et al.*, Report No. FERMILAB-TM-2365, 2007.
  - [18] S. Abachi *et al.* (D0 Collaboration), Nucl. Instrum. Methods Phys. Res. A **338**, 185 (1994).
  - [19] V. M. Abazov *et al.* (D0 Collaboration), Nucl. Instrum. Methods Phys. Res. A **565**, 463 (2006); M. Abolins *et al.* (D0 Collaboration), Nucl. Instrum. Methods Phys. Res. A **584**, 75 (2008); M. Abolins *et al.* (D0 Collaboration), Nucl. Instrum. Methods Phys. Res. A **622**, 298 (2010).
  - [20] R. Engelmann *et al.*, Nucl. Instrum. and Methods **216**, 45 (1983).
  - [21] V. M. Abazov *et al.* (D0 Collaboration), Nucl. Instrum. Methods Phys. Res. A **750**, 78 (2014).
  - [22] T. Sjöstrand, P. Edén, C. Feriberg, L. Lönnblad, G. Miu, S. Mrenna, and E. Norrbin, Computer Phys. Commun. **135**, 238 (2001). PYTHIA version v6.323 is used throughout.
  - [23] J. Pumplin, D. R. Stump, J. Huston, H.-L. Lai, P. Nadolsky, and W.-K. Tung, J. High Energy Phys. **07** 012 (2002); D. Stump, J. Huston, J. Pumplin, W.-K. Tung, H.-L. Lai, S. Kuhlmann, and J. F. Ownes, J. High Energy Phys. **10**, 046 (2003).
  - [24] R. Brun and F. Carminati, CERN Program Library Long Writeup W5013, 1993 (unpublished).
  - [25] P. Golonka and Z. Wąs, Eur. Phys. J. C **45**, 97 (2006).
  - [26] R. Brun and F. Rademakers, Nucl. Instrum. Methods Phys. Res. A **389**, 81 (1997). See also <http://root.cern.ch/>.
  - [27] G. Abbiendi *et al.* (LEP Collaborations ALEPH, DELPHI, L3 and OPAL; SLD Collaboration, LEP Electroweak Working Group, SLD Electroweak and Heavy Flavor Groups), Phys. Rep. **427**, 257 (2006).
  - [28] F. James, CERN Program Program Library Long Writeup D506, 1993 (unpublished).
  - [29] V. M. Abazov *et al.* (D0 Collaboration), Phys. Rev. D **89**, 012005 (2014).
  - [30] R. Hamberg, W. L. van Neerven, and T. Matsuura, Nucl. Phys. **B359**, 343 (1991).
  - [31] S. Jadach, Z. Wąs, R. Decker, and J.H. Kuehn, Computer Phys. Commun. **76**, 361 (1993).
  - [32] V. M. Abazov *et al.* (D0 Collaboration), Phys. Rev. D **84**, 012007 (2011).
  - [33] S. Alioli, P. Nason, C. Oleari, and E. Re, J. High Energy Phys. **07**, 060 (2008).
  - [34] S. Frixione and B. R. Webber, J. High Energy Phys. **06**, 029 (2002).
  - [35] R. D. Ball *et al.*, Nucl. Phys. **B867**, 244 (2013).
  - [36] G. Corcella, I. Knowles, G. Marchesini, S. Moretti, K. Odagiri, P. Richardson, M. Seymour, and B. Webber, J. High Energy Phys. **01**, 010 (2001).
  - [37] A.D. Martin, W. J. Stirling, R. S. Thorne, and G. Watt, Eur. Phys. J. C **63**, 189 (2009).

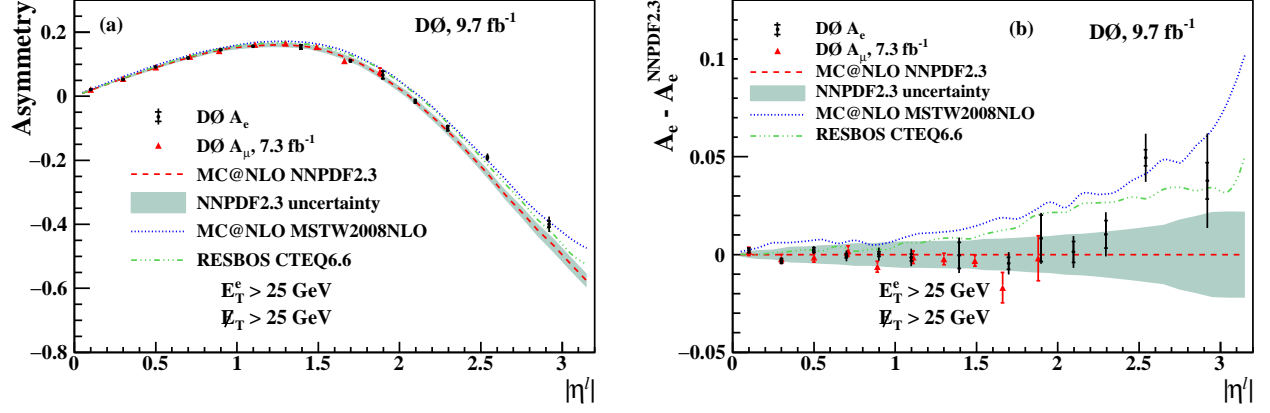


FIG. 13: (color online). The lepton charge asymmetry distribution after CP folding with symmetric kinematic cuts  $E_T^e > 25$  GeV,  $E_T^{\nu} > 25$  GeV. (a) Comparison between the measured asymmetry and predictions and (b) the differences between the data and MC predictions and the predicted central value from MC@NLO using the NNPDF2.3 PDF set. The black dots show the measured electron charge asymmetry, with the horizontal bars showing the statistical uncertainty and the vertical lines showing the total uncertainty. The red triangles show the published D0 muon charge asymmetry [12]. The red dashed lines and cyan bands are the central value and uncertainty band from MC@NLO using the NNPDF2.3 PDF sets. The blue dotted lines show the prediction from MC@NLO using the MSTW2008NLO central PDF set, and the green dot-dashed lines show the prediction from RESBOS using the CTEQ6.6 central PDF set.

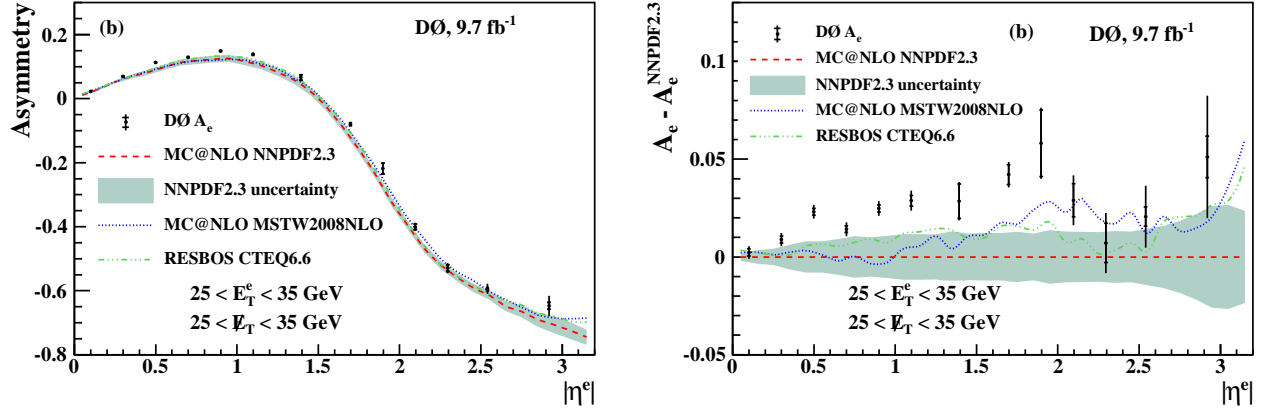


FIG. 14: (color online). The electron charge asymmetry distribution after CP folding with symmetric kinematic cuts  $25 < E_T^e < 35$  GeV,  $25 < E_T^{\nu} < 35$  GeV. (a) Comparison between the measured asymmetry and predictions and (b) the differences between the data and MC predictions and the predicted central value from MC@NLO using the NNPDF2.3 PDF set. The black dots show the measured electron charge asymmetry, with the horizontal bars showing statistical uncertainty and the vertical lines showing the total uncertainty. The red dashed lines and cyan bands are the central value and uncertainty band from MC@NLO using the NNPDF2.3 PDF sets. The blue dotted lines show the prediction from MC@NLO using the MSTW2008NLO central PDF set, and the green dot-dashed lines show the prediction from RESBOS using the CTEQ6.6 central PDF set.

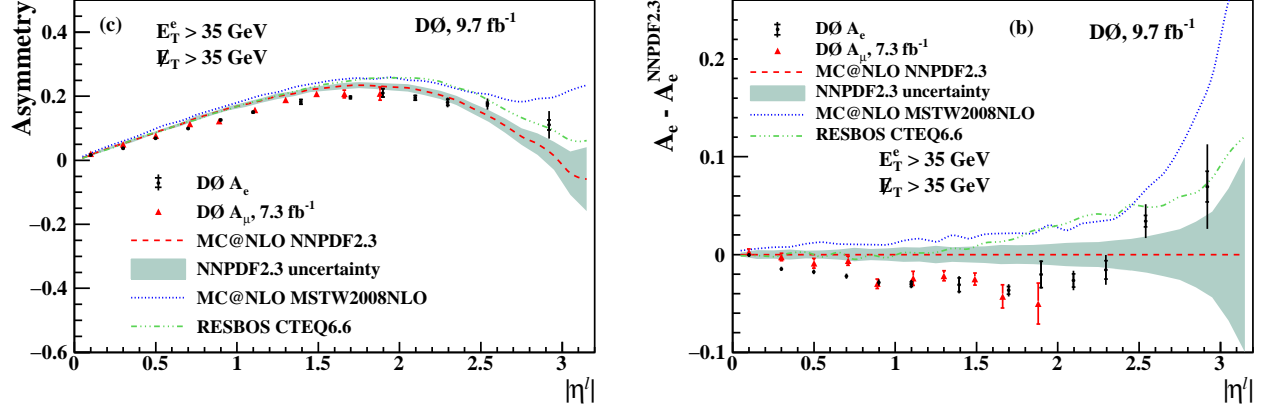


FIG. 15: (color online). The lepton charge asymmetry distribution after CP folding with symmetric kinematic cuts  $E_T^e > 35$  GeV,  $E_T^\mu > 35$  GeV. (a) Comparison between the measured asymmetry and predictions and (b) the differences between the data and MC predictions and the predicted central value from MC@NLO using the NNPDF2.3 PDF set. The black dots show the measured electron charge asymmetry, with the horizontal bars showing statistical uncertainty and the vertical lines showing the total uncertainty. The red triangles show the published D0 muon charge asymmetry [12]. The red dashed lines and cyan bands are the central value and uncertainty band from MC@NLO using the NNPDF2.3 PDF sets. The blue dotted lines show the prediction from MC@NLO using the MSTW2008NLO central PDF set, and the green dot-dashed lines show the prediction from RESBOS using the CTEQ6.6 central PDF set.

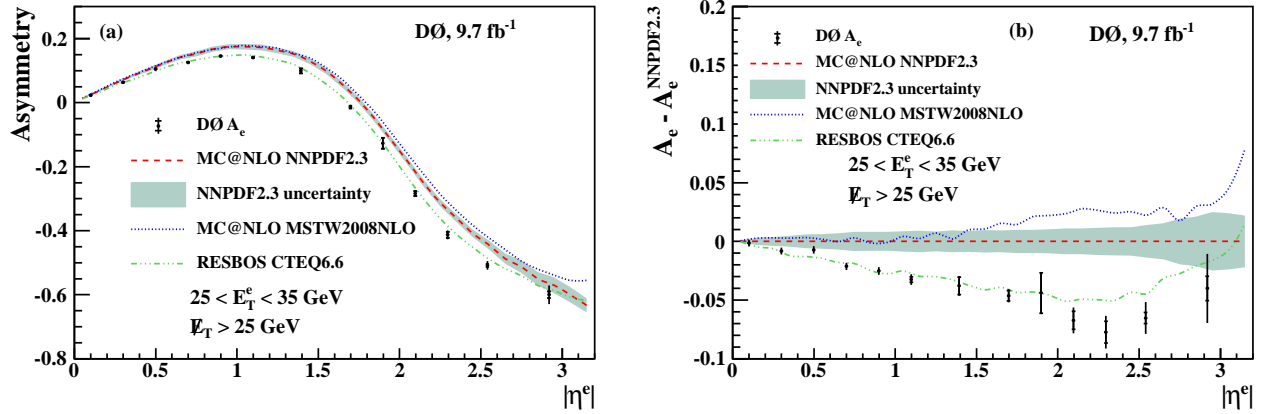


FIG. 16: (color online). The electron charge asymmetry distribution after CP folding with asymmetric kinematic cuts  $25 < E_T^e < 35$  GeV,  $E_T^\mu > 25$  GeV. (a) Comparison between the measured asymmetry and predictions and (b) the differences between the data and MC predictions and the predicted central value from MC@NLO using the NNPDF2.3 PDF set. The black dots show the measured electron charge asymmetry, with the horizontal bars showing statistical uncertainty and the vertical lines showing the total uncertainty. The red dashed lines and cyan bands are the central value and uncertainty band from MC@NLO using the NNPDF2.3 PDF sets. The blue dotted lines show the prediction from MC@NLO using the MSTW2008NLO central PDF set, and the green dot-dashed lines show the prediction from RESBOS using the CTEQ6.6 central PDF set.

FIG. 17: (color online). The electron charge asymmetry distribution after CP folding with asymmetric kinematic cuts  $E_T^e > 35$  GeV,  $\cancel{E}_T > 25$  GeV. (a) Comparison between the measured asymmetry and predictions and (b) the differences between the data and MC predictions and the predicted central value from MC@NLO using the NNPDF2.3 PDF set. The black dots show the measured electron charge asymmetry, with the horizontal bars showing statistical uncertainty and the vertical lines showing the total uncertainty. The red dashed lines and cyan bands are the central value and uncertainty band from MC@NLO using the NNPDF2.3 PDF sets. The blue dotted lines show the prediction from MC@NLO using the MSTW2008NLO central PDF set, and the green dot-dashed lines show the prediction from RESBOS using the CTEQ6.6 central PDF set.

TABLE XV: Correlation matrix of the statistical uncertainties between different  $|\eta^e|$  bins for the kinematic bin  $E_T^e > 25$  GeV,  $E_T > 25$  GeV. The matrix elements are multiplied by 100.

[illegible]

TABLE XVI: Correlation matrix of the statistical uncertainties between different  $|\eta^e|$  bins for the kinematic bin  $25 < E_T^e < 35$  GeV,  $\cancel{E}_T > 25$  GeV. The matrix elements are multiplied by 100.

[illegible]

TABLE XVII: Correlation matrix of the statistical uncertainties between different  $|\eta^e|$  bins for the kinematic bin  $25 < E_T^e < 35$  GeV,  $25 < \cancel{E}_T < 35$  GeV. The matrix elements are multiplied by 100.

[illegible]

TABLE XVIII: Correlation matrix of the statistical uncertainties between different  $|\eta^e|$  bins for the kinematic bin  $E_T^e > 35$  GeV,  $\cancel{E}_T > 25$  GeV. The matrix elements are multiplied by 100.

$ \eta^e $ bins	1	2	3	4	5	6	7	8	9	10	11	12	13
1	100	0.75	0.00	0.00	0.00	0.00	0.00	0.00	0.00	0.00	0.00	0.00	0.00
2		100	0.68	0.00	0.00	0.00	0.00	0.00	0.00	0.00	0.00	0.00	0.00
3			100	0.65	0.00	0.00	0.00	0.00	0.00	0.00	0.00	0.00	0.00
4				100	0.65	0.00	0.00	0.00	0.00	0.00	0.00	0.00	0.00
5					100	0.63	0.00	0.00	0.00	0.00	0.00	0.00	0.00
6						100	0.31	0.00	0.00	0.00	0.00	0.00	0.00
7							100	0.52	0.00	0.00	0.00	0.00	0.00
8								100	0.51	0.00	0.00	0.00	0.00
9									100	0.05	0.00	0.00	0.00
10										100	0.39	0.00	0.00
11											100	0.16	0.00
12												100	0.32
13													100

TABLE XIX: Correlation matrix of the statistical uncertainties between different  $|\eta^e|$  bins for the kinematic bin  $E_T^e > 35$  GeV,  $\cancel{E}_T > 35$  GeV. The matrix elements are multiplied by 100.

$ \eta^e $ bins	1	2	3	4	5	6	7	8	9	10	11	12	13
1	100	0.75	0.00	0.00	0.00	0.00	0.00	0.00	0.00	0.00	0.00	0.00	0.00
2		100	0.67	0.00	0.00	0.00	0.00	0.00	0.00	0.00	0.00	0.00	0.00
3			100	0.65	0.00	0.00	0.00	0.00	0.00	0.00	0.00	0.00	0.00
4				100	0.64	0.00	0.00	0.00	0.00	0.00	0.00	0.00	0.00
5					100	0.62	0.00	0.00	0.00	0.00	0.00	0.00	0.00
6						100	0.31	0.00	0.00	0.00	0.00	0.00	0.00
7							100	0.53	0.00	0.00	0.00	0.00	0.00
8								100	0.38	0.00	0.00	0.00	0.00
9									100	0.07	0.00	0.00	0.00
10										100	0.41	0.00	0.00
11											100	0.16	0.00
12												100	0.35
13													100

TABLE XX: The fraction of events in each reconstruction-level kinematic bin that come from different generator-level kinematic bins. These bins are not all independent.

	$20 < p_T^e < 25$ OR $20 < p_T^\nu < 25$	$p_T^e > 25$ AND $p_T^\nu > 25$	$25 < p_T^e < 35$ AND $p_T^\nu > 25$	$25 < p_T^e < 35$ AND $25 < p_T^\nu < 35$	$p_T^e > 35$ AND $p_T^\nu > 25$	$p_T^e > 35$ AND $p_T^\nu > 35$
$20 < E_T^e < 25$ OR $20 < \cancel{E}_T < 25$	0.64	0.36	0.32	0.27	0.04	0.02
$E_T^e > 25$ AND $\cancel{E}_T > 25$	0.08	0.92	0.35	0.22	0.57	0.42
$25 < E_T^e < 35$ AND $\cancel{E}_T > 25$	0.12	0.88	0.80	0.51	0.08	0.06
$25 < E_T^e < 35$ AND $25 < \cancel{E}_T < 35$	0.15	0.85	0.79	0.60	0.06	0.03
$E_T^e > 35$ AND $\cancel{E}_T > 25$	0.05	0.95	0.06	0.03	0.89	0.66
$E_T^e > 35$ AND $\cancel{E}_T > 35$	0.03	0.97	0.05	0.02	0.92	0.72